

# Analysis of Lattice and Continuum Models of Bioactive Porous Media\*

Andrew L. Krause<sup>†</sup>, Dmitry Beliaev<sup>†</sup>, Robert A. Van Gorder<sup>†</sup>, and Sarah L. Waters<sup>†</sup>

**Abstract.** In the context of tissue engineering, we recently proposed a lattice model for a bioactive porous tissue scaffold in order to understand the role of an active pore network in tissue growth [*Lattice and Continuum Modelling of a Bioactive Porous Tissue Scaffold*, preprint, 2017]. This model considered the scaffold as an evolving lattice of pores, with coupling between local cell growth in the pores, and fluid flow through the medium. Here we consider a variant of this lattice model as well as a spatially continuous analogue. We analyze these models from a dynamical systems perspective emphasizing qualitative changes in model behaviour as parameters are varied. Depending on the size of the underlying network, we observe oscillations and steady states in cell density exhibited in both models. Steady state behaviour can be described in large cell diffusion regimes via regular asymptotic expansions in the diffusion parameter. We numerically continue steady state solutions into intermediate diffusion regimes, where we observe symmetry-breaking bifurcations to both oscillatory and steady state behaviours that can be explained via local bifurcations, as well as symmetry-preserving oscillations that do not bifurcate from steady states. The spatially continuous analogue of the model only exhibits symmetric steady states and oscillatory solutions, and we conjecture that it is the finite lattice that gives rise to the more complicated symmetry-breaking dynamics. We suggest that the origin of both types of oscillations is a nonlocal reaction-diffusion mechanism mediated by quasi-static fluid flow. Finally we relate these results back to the original modelling question of how network topology influences tissue growth in a bioactive porous tissue scaffold.

**Key words.** bioactive porous media, lattice and continuum models, Hopf bifurcations, nonlocal reaction-diffusion equations

**1. Introduction.** Tissue engineering, a multidisciplinary field seeking to create tissues and organs *de novo*, is rapidly growing in part due to an increasing demand for medical uses in transplantation and testing [3]. A major challenge in tissue engineering is to properly understand and exploit processes that occur at very different spatial and temporal scales in order to develop successful artificial tissues. Mathematical modelling has been increasingly used to understand these complex physical and biological processes, and hence underpins experimental work in tissue engineering [20, 26]. In addition to providing conceptual understanding, such modelling is used to predict and optimize bioreactor operating regimes which saves on costly and time-consuming experimental trials.

In [12] we introduced two models of a two-dimensional porous tissue scaffold within a perfusion bioreactor. Our models incorporated interactions between a viscous fluid phase representing a culture medium, and a cell phase modelling the biomass of proliferating cells and their extracellular matrix. These phases interact as the cells are assumed to die if the local fluid shear stress becomes too large, and they were assumed to block pores, reducing the local permeability of the scaffold, as the cell density increased. We modelled this process using a

---

\*Submitted to the editors DATE.

**Funding:** FUNDING

<sup>†</sup>Mathematical Institute, Andrew Wiles Building, University of Oxford, Radcliffe Observatory Quarter, Woodstock Rd, OX2 6GG, UK. (Andrew.Krause@maths.ox.ac.uk, Dmitry.Beliaev@maths.ox.ac.uk, Robert.VanGorder@maths.ox.ac.uk, Sarah.Waters@maths.ox.ac.uk).

continuum approach involving a system of PDEs, and a lattice approach involving a spatially embedded network of ODEs, and discussed quantitative and qualitative differences between these approaches. While lattice approaches exist in related biological literature [1, 17, 24], they have not been fully explored to understand the impact of finite pore networks on porous media whose structure changes due to cell growth. This is particularly true in terms of non-equilibrium dynamics exhibited by these models. Continuum models for fluid flow in porous media can be justified for pore networks with many pores, corresponding either to large or very porous materials [2]. Many current tissue scaffolds used experimentally, however, have pore sizes and scaffold geometries such that the number of pores is of order  $O(1,000)$  or less; see Figure 6 of [8] for an example and [9, 14, 25] for general discussions of pore size, scaffold geometry, and transport phenomena in porous tissue scaffolds. These experimental considerations motivate our study of finite lattice models.

In this paper we modify the model presented in [12] to investigate similar interactions between fluid flow and cell proliferation. Specifically, we assume that cells die due to high pressures, rather than fluid shear stress. This is motivated in part by computational modelling of cell death due to hydrostatic pressure [19], and by experimental work demonstrating cell death due to pressure such as [16]. In addition to these physical considerations, these modified models are more amenable to mathematical and numerical investigation due to simpler coupling between the flow and growth processes. This allows for a more thorough discussion of long-time non-equilibrium solutions observed in the models in [12], as well as some analytical results. In the shear stress model presented there, oscillatory solutions were only present for the lattice model, and were more pronounced for smaller pore networks. In contrast in the present paper, we observe the existence of oscillatory behaviour in both lattice and continuum models, and exploit this as a basis for understanding the mathematical mechanisms leading to oscillatory behaviour in the original model. Additionally, the number and structure of steady states we find in this model is much smaller, allowing for a dimensional reduction of the model that captures many salient features of the dynamics.

In Section 2, we present the two models of the same form as [12], briefly discussing their assumptions and components. We also present one-dimensional (1-D) reduced models of the full two-dimensional (2-D) equations. This allows for a solution of the flow problems reducing the full system to a scalar nonlocal reaction-diffusion equation for the spatially continuous model, and an analogous strongly coupled system of ODEs for the lattice. In Section 3, we present a broad comparison between the lattice and continuum models in terms of quantitative predictions as well as typical solution behaviours, which we find numerically. In Section 4, we derive asymptotic solutions for large values of the diffusion parameter as a way of bounding the region in parameter space where we anticipate non-equilibrium behaviour. In Section 5, we describe the more complicated dynamics outside of this asymptotic regime by presenting numerical bifurcation diagrams of large and small lattices, as well as the continuum model. Using these diagrams we broadly characterize the steady states and oscillatory asymptotic states by their symmetry. We exhibit continuation results showing the existence of Hopf and pitchfork bifurcations that break vertical symmetry of solutions, and suggest that a different kind of oscillation, which preserves this symmetry, is not due to a local bifurcation from a steady state. Finally, we give an overview of these results in Section 6, and discuss the implications for further modelling of porous scaffolds used in tissue engineering.

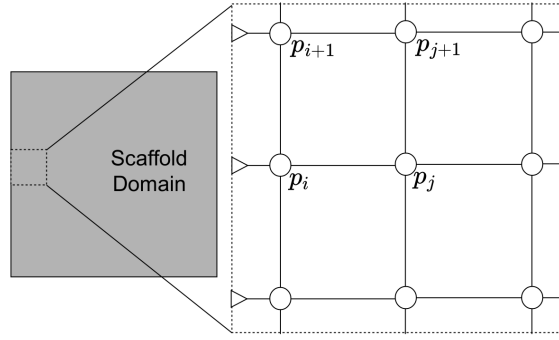


Figure 1: A representation of the lattice domain.

**2. Description of the Models.** We recall the models presented in [12], beginning with the lattice model. We consider a square lattice of  $n$  nodes per side, and at each node define a pressure  $p_i$  and a cell density  $N_i$ . Figure 1 is a representation of this lattice as a model for a porous scaffold. For the notation on the square lattice, we label nodal variables with single indices, counting from the bottom-left upwards so that  $p_1$  is the pressure at the bottom-left node, and  $p_{n^2}$  is the pressure at the top-right node. The adjacency matrix  $A$  has the form  $A_{ij} = A_{ji} = 1$  if nodes  $i$  and  $j$  are connected, and  $A_{ij} = 0$  otherwise. We write the graph Laplacian as the matrix  $L$  such that  $\sum_j A_{ij}(v_i - v_j) = \sum_j L_{ij}v_i$ . See [18] (and references therein) for a discussion of networks in general and properties of these matrices.

We assume the fluid is viscous, Newtonian, and incompressible. We model the flow rate between nodes  $i$  and  $j$  via Poiseuille flow in a pipe of radius  $R_{ij}$  which depends on the cell density at these two nodes. We assume that a constant fluid flow enters the domain from the left and is allowed to leave the domain along the right side of the lattice. We use pressures  $\tilde{p}_i$  computed from a unit pressure drop problem to compute the physical pressure at each node by rescaling to match the total flow through the boundaries by computing the flow given by the unit pressure drop  $Q$ . See [12] for details of this rescaling procedure. Our system of non-dimensional equations is then

$$(1) \quad \sum_{j=1}^{n^2} A_{ij} R_{ij}^4 (\tilde{p}_i - \tilde{p}_j) = \begin{cases} 1 - \tilde{p}_i, & 1 \leq i \leq n, \\ 0, & n < i \leq n^2 - n, \\ -\tilde{p}_i, & n^2 - n < i \leq n^2, \end{cases}$$

$$(2) \quad \frac{dN_i}{dt} = F_1(p_i)N_i(1 - N_i) - F_2(p_i)N_i + \delta n^2 \sum_{j=1}^{n^2} A_{ij}(N_j - N_i),$$

$$(3) \quad R_{ij} \equiv R(N_i, N_j) = 1 - \frac{\rho}{2}(N_i + N_j), \quad Q = \sum_{i=1}^n 1 - \tilde{p}_i, \quad \mathbf{p} = \tilde{\mathbf{p}} \frac{1}{Q},$$

$$(4) \quad F_1(p_i) = 1 - \left(\frac{1}{2}\right) (\tanh[g(p_i - p_l)] + 1), \quad F_2(p_i) = \left(\frac{1}{2}\right) (\tanh[g(p_i - p_l)] + 1),$$

where  $\delta, \rho, g, p_l > 0$  are constants. Equations (1) represent conservation of mass enforced at

each node, with a pressure drop across the square domain. Equations (2) describe logistic cell growth and death modulated by the functions  $F_1$  and  $F_2$  of the pressure at that node, along with cell diffusion between nodes. Equations (3) describe how the presence of cells influences flow via reducing pipe radii, and a rescaling procedure to conserve total fluid flow into the domain. Equations (4) describe functions of the pressure chosen to model a ‘proliferation’ and a ‘death’ response of the cells to low and high levels of fluid pressure respectively. The use of hyperbolic tangent functions is a modelling choice following [22], although similar choices such as step functions and mollified step functions have been used elsewhere [7]. See [12] for further details.

The analogous continuum model we will compare this to can be written,

$$(5) \quad \mathbf{u} = -k(N)\nabla\tilde{p}, \quad \nabla \cdot \mathbf{u} = 0,$$

$$(6) \quad \frac{\partial N}{\partial t} = F_1(p)N(1 - N) - F_2(p)N + \delta\nabla^2 N,$$

$$(7) \quad Q = \int_0^1 -k(N(0, \hat{y}, t)) \frac{\partial p}{\partial x}(0, \hat{y}) d\hat{y}, \quad p = \frac{\tilde{p}}{Q_d}, \quad k(N) = (1 - \rho N)^4,$$

$$(8) \quad F_1(p) = 1 - \left(\frac{1}{2}\right) (\tanh[g(p - p_c)] + 1), \quad F_2(p) = \left(\frac{1}{2}\right) (\tanh[g(p - p_c)] + 1),$$

where  $\delta$ ,  $\rho$ ,  $g$ , and  $p_c$  are positive real constants. We prescribe the boundary and initial conditions

$$(9) \quad \mathbf{u} \cdot \mathbf{n} = 0 \text{ at } y = 0, 1, \quad \tilde{p} = 1 \text{ at } x = 0, \quad \tilde{p} = 0 \text{ at } x = 1,$$

$$(10) \quad \mathbf{n} \cdot \nabla N = 0 \text{ for } \mathbf{x} \in \partial[0, 1]^2, \quad N(x, y, 0) = N_0(x, y).$$

Here both models have no-flux or Neumann conditions on all boundaries for the cell density, and on the horizontal boundaries for the fluid. To describe solutions with certain symmetries, we also consider 1-D models below without horizontal boundaries, as well as periodic conditions on both cell density and fluid flux along the horizontal boundaries. For the lattice, these conditions are encoded in the adjacency matrix  $A_{ij}$  by adding edges along these boundary components.

**2.1. Model Simplifications.** We can simplify the lattice equations by eliminating the rescaling of the pressure. We start by replacing  $\tilde{p}_i$  with  $p_i$  using the second equation of (3) to find in Equation (1),

$$(11) \quad \sum_{j=1}^{n^2} A_{ij} R_{ij}^4 (p_i - p_j) = \begin{cases} \frac{1}{Q} - p_i, & 1 \leq i \leq n, \\ 0, & n < i \leq n^2 - n, \\ -p_i, & n^2 - n < i \leq n^2, \end{cases}$$

where we can now solve for  $Q$  in terms of  $p_i$ ,

$$Q = \sum_{j=1}^n 1 - \tilde{p}_j = n - Q \sum_{j=1}^n p_j,$$

which implies,

$$Q = \frac{n}{1 + \sum_{j=1}^n p_j}.$$

Using this expression for  $Q$ , our system of fluid equations (11) becomes

$$(12) \quad \sum_{j=1}^{n^2} A_{ij} R_{ij}^4 (p_i - p_j) = \begin{cases} \frac{1}{n} \left( 1 + \sum_{j=1}^n p_j \right) - p_i, & 1 \leq i \leq n, \\ 0, & n < i \leq n^2 - n, \\ -p_i, & n^2 - n < i \leq n^2. \end{cases}$$

With this simplification, we can solve the pressure equations when the cell densities (and hence the pressures) are homogeneous vertically. We label the value at a representative node by  $p_i \equiv \hat{p}_k$  for  $k = \lfloor \frac{i-1}{n} \rfloor + 1$ . So the first  $n$  variables have the value  $\hat{p}_1$ , the next  $n$  have the value  $\hat{p}_2$ , etc. We analogously denote the cell densities as  $\hat{N}_i$  at node  $i$ . We rewrite Equation (12) using these variables as

$$(13) \quad \sum_{j=1}^{n^2} \hat{A}_{ij} R^4(\hat{N}_i, \hat{N}_j) (\hat{p}_i - \hat{p}_j) = \begin{cases} \frac{1}{n}, & i = 1, \\ 0, & 1 < i < n, \\ -\hat{p}_n, & i = n, \end{cases}$$

where we have used the simplification  $\frac{1}{n}(1 + \sum_{j=1}^n p_j) - p_i = \frac{1}{n}(1 + n\hat{p}_1) - \hat{p}_1 = \frac{1}{n}$ . The adjacency matrix  $\hat{A}_{ij}$  represents the path graph on  $n$  vertices. An equivalent way of writing this system is

$$(14) \quad \begin{aligned} R^4(\hat{N}_1, \hat{N}_2) (\hat{p}_1 - \hat{p}_2) &= \frac{1}{n}, \\ R^4(\hat{N}_i, \hat{N}_{i+1}) (\hat{p}_i - \hat{p}_{i+1}) + R^4(\hat{N}_i, \hat{N}_{i-1}) (\hat{p}_i - \hat{p}_{i-1}) &= 0, \quad 1 < i < n, \\ R^4(\hat{N}_n, \hat{N}_{n+1}) (\hat{p}_n - \hat{p}_{n-1}) &= -\hat{p}_n. \end{aligned}$$

Adding all  $n$  equations in (14) we find that  $\hat{p}_n = \frac{1}{n}$ , where we have used the symmetry of the function  $R$ . Now for  $1 \leq i < n$  we can iteratively solve these equations to find

$$(15) \quad \hat{p}_i = \frac{1}{n} \left( 1 + \sum_{k=i}^{n-1} R^{-4}(\hat{N}_k, \hat{N}_{k+1}) \right).$$

This is equivalent to saying that resistance in serial circuits is additive, where this pressure variable is playing the role of voltage and  $R^{-4}(\hat{N}_k, \hat{N}_{k+1})$  is the resistance between nodes  $k$  and  $k+1$ .

This simplification extends to the PDE system with the same symmetry. We assume that the cell density varies only in the  $x$  direction, so that the permeability  $k = k(N(x))$  also only varies in this direction, where we are suppressing the time dependence of the cell density as the pressure is quasi-static. By the symmetry of the boundary conditions we have that  $\tilde{p} = \tilde{p}(x)$ , so our governing flow equations become

$$(16) \quad 0 = \partial_x(k(x)\partial_x\tilde{p}), \quad Q = -k(N(0))\frac{\partial\tilde{p}}{\partial x}(0), \quad p = \frac{\tilde{p}}{Q_d}.$$

Integrating the first of these we find the pressure as

$$(17) \quad \tilde{p}(x) = D \int_1^x \frac{1}{k(N(\alpha))} d\alpha + C,$$

for some constants  $C$  and  $D$ . Using the boundary conditions (9) we have that

$$(18) \quad \tilde{p}(x) = \frac{\int_x^1 \frac{1}{k(N(\alpha))} d\alpha}{\int_0^1 \frac{1}{k(N(\alpha))} d\alpha}.$$

Finally using the rescaling in the second equation of (16) we find our pressure solution becomes

$$(19) \quad p(x) = \int_x^1 \frac{1}{k(N(\alpha))} d\alpha.$$

If we substitute (19) into Equation (6) we obtain a single equation for the cell density,

$$(20) \quad \frac{\partial N}{\partial t} = F_1 \left( \int_x^1 \frac{1}{k(N(\alpha))} d\alpha \right) N(1-N) - F_2 \left( \int_x^1 \frac{1}{k(N(\alpha))} d\alpha \right) N + \delta \partial_x^2 N.$$

Equation (20) is a spatially nonlocal scalar reaction-diffusion equation for the cell density  $N$ .

**2.2. Bounded Dynamics.** We consider solutions to Equations (1)-(4) with initial conditions  $N_i(0) \in [0, 1]$  for all  $1 \leq i \leq n^2$ . We note that for all  $p \in \mathbb{R}$ , the functions in Equations (4) are bounded as  $0 \leq F_1(p) \leq 1$  and  $0 \leq F_2(p) \leq 1$ . Now we assume that for some  $t^*$ ,  $N_i(t^*) \in [0, 1]$  for all  $i$ , and  $N_k(t^*) = 1$  for some  $k$ . We then have that

$$(21) \quad \frac{dN_k}{dt} = -F_2(p_k) + \delta n^2 \sum_{j=1}^{n^2} A_{kj}(N_j - 1) \leq 0,$$

Hence continuously differentiable ( $C^1$ ) solutions to Equations (2) are bounded above.

Similarly, assume that for some  $t^*$ ,  $N_i(t^*) \in [0, 1]$  for all  $i$ , and that  $N_m(t^*) = 0$  for some  $m$ . We then have that,

$$(22) \quad \frac{dN_m}{dt} = \delta n^2 \sum_{j=1}^{n^2} A_{mj}(N_j) \geq 0,$$

and so continuously differentiable solutions are also bounded below. Note that these bounds are independent of the pressures  $p_i$ . So we have that  $N_i(t) \in [0, 1]$  for all  $i$  and for all  $t \geq 0$ . Equation (15) can then be used to explicitly bound the (1-D) pressures  $p_i$  in terms of  $n$ ,  $\rho$  and the extremal values of  $N_i$ .

While the authors are not aware of a formal comparison principle applicable to Equations (5)-(10), the above argument gives a heuristic bound on the behaviour of solutions for these equations as well. The existence of spatiotemporal oscillations suggests that a general comparison principle is not directly applicable, and hence a rigorous treatment of Equations (5)-(10) would be needed in order to formally extend this argument.

**3. Numerical Exploration of Solution Behaviours.** In this section we present numerical solutions for the lattice equations (1)-(4) as well as the PDE system given by (5)-(10). For these simulations we fix  $\rho = 0.9$  so that cell growth significantly affects the effective permeability of the medium. To capture sufficiently sharp behaviour in the pressure functions, we set  $g = 60$ . The other parameters are varied to demonstrate different solution behaviours.

The PDE model was simulated using the finite element software COMSOL with 24,912 triangular elements, as well as a finite difference scheme implementing the same model. The lattice model was solved using an explicit adaptive Runge-Kutta method, ‘ode45’ in MATLAB, with a maximal time step of  $10^{-3}$ . The restriction of the maximal time step was to ensure a good approximation of bifurcation phenomena [6].

From Section 2.2 we have that the cell densities are bounded, so that for any  $t > 0$  we have  $0 \leq N_i(t) \leq 1$  and  $0 \leq N(x, y, t) \leq 1$ , if the initial data are similarly bounded. From this and the monotonicity of Equations (15) and (19), we can compute the maximum and minimum pressures throughout the domain in each model. We then deduce the ranges of the pressure threshold parameters  $p_l$  and  $p_c$  that give rise to non-trivial long-time dynamics. Specifically we consider ranges of these threshold parameters as  $1/n < p_l < 1/n + (1 - \rho)^{-4} \approx 10,000$  for the lattice and  $0 < p_c < (1 - \rho)^{-3} = 1,000$  for the PDE. This allows us to explore dynamics that are not the trivial states of either uniform cell death or logistic cell growth to a uniform carrying capacity. Because of the difference in the orders of magnitude between these two ranges, which is due to the constitutive difference between Poiseuille flow and cubic permeability in Darcy’s law, we relate the PDE pressure threshold as  $p_c = p_l/10$  when we compare the two models. This is a crude comparison but it does give some insight into the effects of these constitutive parameters. See [12] for a discussion of why these constitutive exponents differ between the models. Changing the exponent in the permeability, the third equation in (7), from 3 to 4 gives qualitatively similar behaviour for the PDE.

For small initial cell densities, the lattice and PDE models are both insensitive to changes in initial conditions. For all of our simulations, we set the initial data to be a perturbed uniform state so that  $N_0(x, y) \approx 0.1$  and  $N_i(0) \approx 0.1$ . The cell densities grow uniformly until the pressure at some point of the domain reaches the threshold  $p_c$  for the PDE or  $p_l$  for the lattice, where some regions then locally experience cell death due to high pressure. The simulations then tend to a spatial horizontal gradient with low cell density on the left side of the lattice (where the pressure is highest) and high cell density on the right side of the lattice (where the pressure is lowest). We observed one of three different long time behaviours: a stable steady state, a vertically-symmetric ‘pulsating’ oscillation, or a non-



vertically symmetric oscillation. The steady states observed were either vertically symmetric, or non-vertically symmetric. The latter was only observed in lattice simulations with  $n \lesssim 50$ .

At large values of  $\delta$ , or large threshold parameters  $p_l$  or  $p_c$ , all simulations tend to a similar steady state with a gradual gradient in cell density. In Figure 2 we plot two example cell density distributions alongside corresponding plots of pressure. We also plot time series of the nodal evolution along the diagonals of the scaffold, i.e. all nodes along the lines  $x = y$  and  $x = 1 - y$ . For large  $\delta$ , there is a non-negligible cell density present in the region of high pressure despite the local cell density being governed by exponential death. The pressure does not vary significantly in this region of lower cell density near the left side of the scaffold, as the effective permeability changes little due to low cell densities. In these parameter ranges, the 1-D reduction described in Section 2.1 is a quantitatively accurate approximation. We conjecture that these solutions obey a vertical symmetry on the lattice. This symmetry can be described by the group of permutations on  $n$  symbols,  $S_n$ , as any row of nodes can be interchanged with any other without changing the solution.

For smaller values of the diffusion we observe a different long-time behaviour. In Figure 3 we plot the cell density over the domain at two different points in time for a large lattice of size  $n = 100$  and the PDE model. Here the cell density throughout the scaffold oscillates with a global ‘pulsing’ from the right to the left side of the domain. The amplitude of the oscillation in the mean cell density in the PDE is smaller than in the lattice. In Figure 4 we show the cell densities across diagonal nodes for these two cases, and observe stable oscillations at each node throughout the domain. The lattice simulation has the largest nodal oscillation amplitudes at the far left of the lattice, and these nodes never get close to the zero steady state, whereas the PDE simulation has its largest oscillations in the middle of the domain, and the far leftmost part of the domain has become devoid of cells. Both kinds of behaviour can be found in each model, but in our simulations the lattice model was more likely to not have a ‘dead’ region of the domain, whereas when the PDE solutions did exhibit oscillations, they did have this region. These large oscillations persist in the 1-D reductions of both models, as well as when the horizontal boundary conditions for cells and fluid flow are changed from Neumann to periodic conditions. This suggests that these oscillations are inherently a 1-D phenomenon.

Qualitatively different steady states and oscillations exist in the smaller lattices. In many of our simulations of smaller lattices, we observe a complicated breaking of the vertical symmetry seen in the previous two kinds of asymptotic behaviour. In Figure 5 we give an example of one of these non-vertically symmetric oscillations. The cell density oscillates vertically like a wave being reflected from the two impermeable boundaries. Note that the time series in Figure 5e separates into ‘bands.’ These correspond to columns in the lattice (shown in Figures 5a-5d). The largest of these bands that changes between a growing and a dying state (shown in red and green in Figure 5e) corresponds to the third column from the right boundary in the lattice. These oscillations are more complicated than the large pulsing ones discussed previously, as their existence depends on the number of nodes  $n$  of the lattice in addition to the boundary conditions. We note that the mean cell density during an oscillation, plotted in Figure 5f, has many turning points despite being periodic. For this particular parameter set, changing the horizontal boundary conditions from no-flux on the fluid and cells to periodic conditions eliminated the oscillations. Similarly, the 1-D model did not oscillate for these



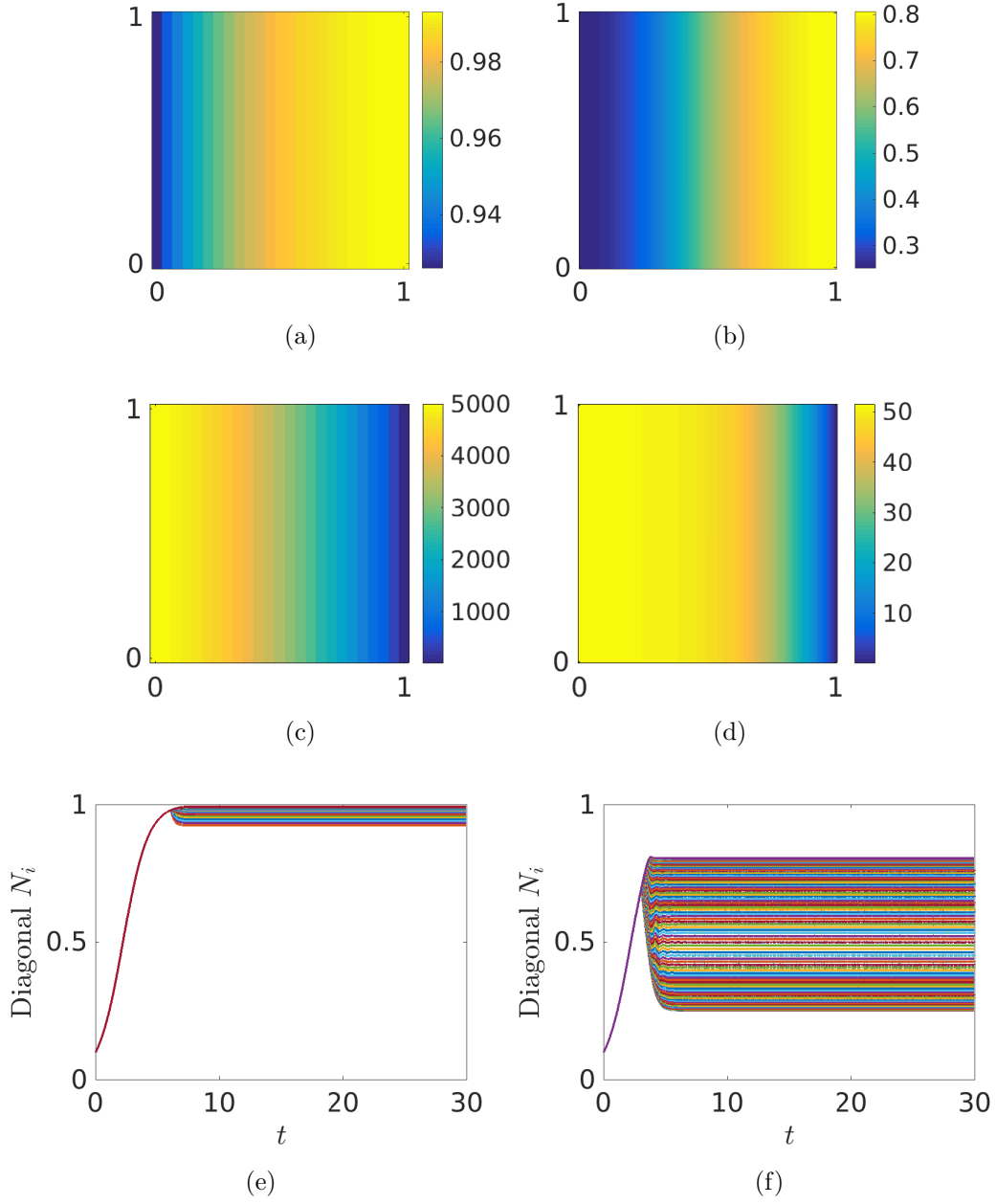


Figure 2: Cell density plots in (a)-(b), pressure plots in (c)-(d) at  $t = 30$  for  $\delta = 10^{-1}$ , and time series showing the evolution from uniform growth to these stationary patterns in (e)-(f). Plots (a), (c) and (e) correspond to simulations with  $p_l = 50$ , with  $n = 50$  and plots (b), (d), and (f) correspond to simulations with  $p_l = 5000$  with  $n = 100$ .

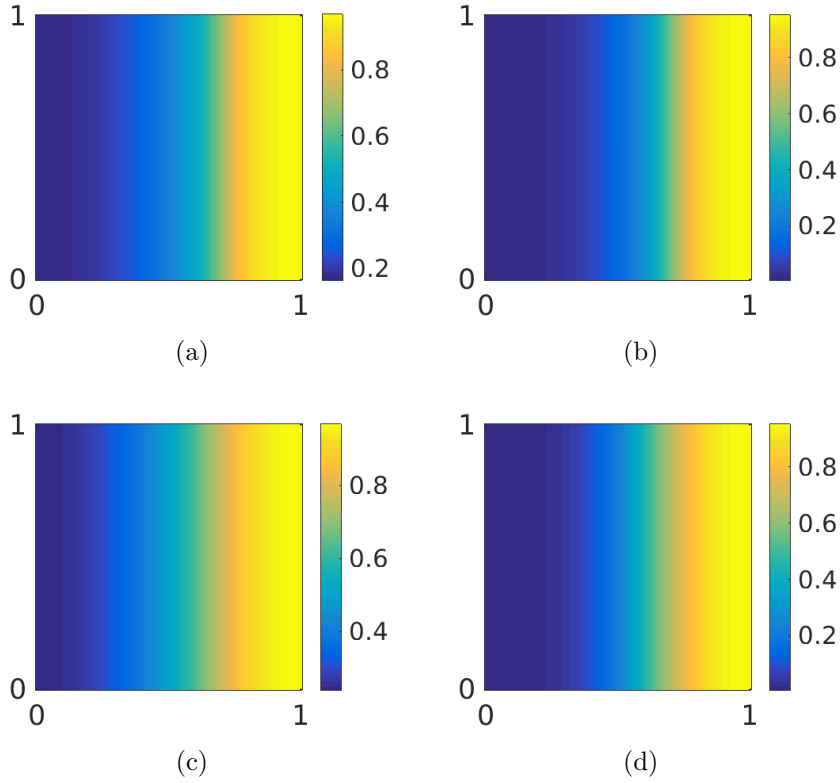


Figure 3: Plots (a) and (c) are of cell density for a lattice of size  $n = 100$ ,  $\delta = 10^{-2}$ ,  $p_l = 500$  at times  $t = 28.42$  in (a), and  $t = 27.9$  in (b). Plots (b) and (d) are of cell density for the PDE with  $\delta = 10^{-2}$ ,  $p_c = 50$  at times  $t = 27.24$  in (b), and  $t = 27.76$  in (d).

parameters.

In Figure 6 we demonstrate non-symmetric oscillations in a larger lattice. We plot the cell density at every node and demonstrate a similar oscillation as in Figure 5. We also show the effect of changing the horizontal boundary conditions to periodic for both the fluid and the cell density, and for the 1-D model. The periodic conditions change the oscillation to have the profile of a travelling wave through any vertical column through the lattice. The 1-D model does not oscillate and instead reaches a steady state. Note that the ‘bands’ in Figure 6 correspond to single columns of nodes.

For even larger lattices we observe combinations of both kinds of oscillations. In Figure 7a, the cell densities settle into a non-symmetric steady state, whereas in Figure 7b the cell densities continue to show pulsing oscillations in combination with non-symmetric oscillations. The 1-D variant of Figure 7b exhibits pulsing oscillations to confirm that the underlying symmetrical oscillation exists in this system. We conjecture that the non-vertically symmetric oscillations will be observed less frequently as the number of nodes increases, and that the larger pulsing oscillations (along with vertically-symmetric steady states) will become more

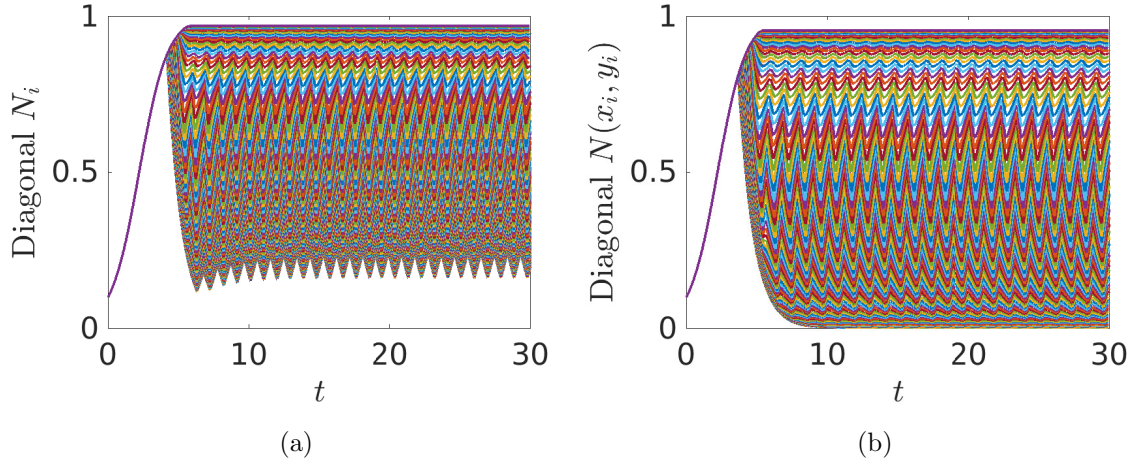


Figure 4: Time series of nodal values of the cell density for a lattice of size  $n = 100$ ,  $\delta = 10^{-2}$ ,  $p_l = 500$  in (a), and along 200 corresponding diagonal interpolants of the PDE system with  $\delta = 10^{-2}$ ,  $p_c = 50$  in (b).

common in a sense that we describe in Section 5.

We quantitatively compare these simulations in terms of mean cell density. We assume that after  $t = 20$  time units that the cell density is close to its asymptotic state (either a steady state or a limit cycle). To account for variations due to oscillatory behaviour, we average over the last 10 time units (after the transient 20 time unit period) and plot the spatial mean of the cell density for each simulation in Figure 8. The colours correspond to the thresholds  $p_c = p_l/10$ , and the symbols to the various lattice sizes and the PDE. We note that the diffusion  $\delta$  and the pressure threshold largely determine the mean cell density. For  $\delta = 10^{-2}$  in particular, the lattice size plays a significant role. We analytically approximate the larger  $\delta$  values in Section 4 asymptotically.

We broadly compare the effect of the oscillations on the mean cell density. We compute the maximum and minimum values that the mean cell density takes in the last 10 time units after a transient period of  $t = 20$  time units has elapsed. We plot the difference between these values in Figure 9, using the same symbols and colours to denote the simulations as in Figure 8. This gives a measure of the quantitative effect these oscillations would have on experimental observables, such as permeability and total cell density. We also observe some interesting variations in the amplitude of these oscillations, such as a non-monotonic dependence on both  $\delta$  and the thresholds for different models. All of the simulations with large oscillations in mean cell density in this plot (e.g. above the value of 0.03) corresponded to large pulsing oscillations, and were quantitatively comparable to their 1-D counterparts. The non-vertically symmetric oscillations have only a small effect on changes in mean cell density, whereas the vertically symmetric oscillations have a potentially measurable effect on global properties of the scaffold.

Some simulations exhibit excitable dynamics. In Figure 10a we first show the evolution

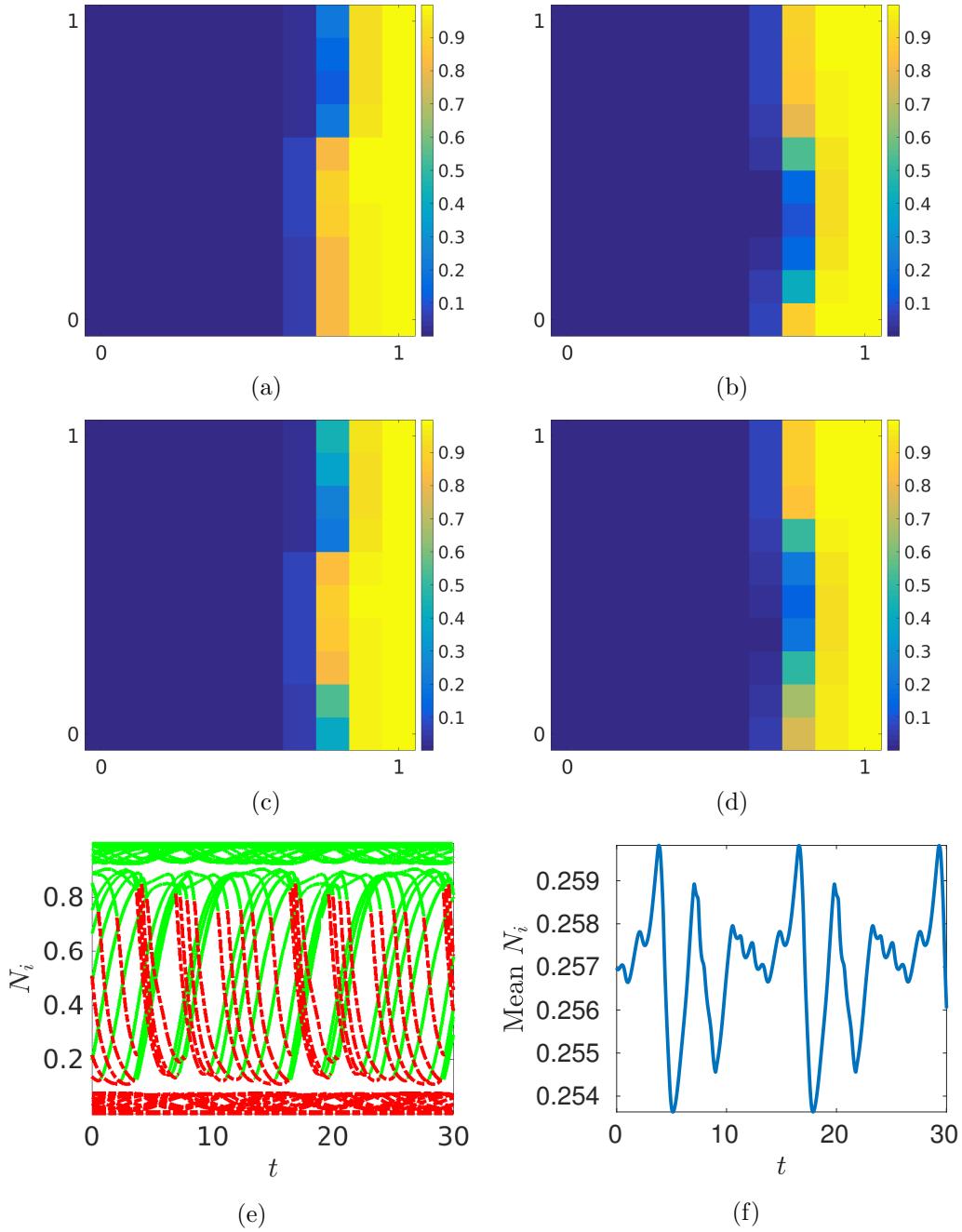


Figure 5: Plots of cell density for a lattice of size  $n = 10$ ,  $\delta = 10^{-3}$ ,  $p_l = 500$  at times  $t = 15$ ,  $t = 20$ ,  $t = 25$ , and  $t = 30$  in (a)-(d) respectively. We plot the nodal values of the cell density at every node in the lattice in (e) where the line is colored green if  $p_i < p_l$  and red if  $p_i > p_l$ . In (f) we plot the mean cell density during the oscillations. Note that we have only shown time series for latter time periods after the cell densities have settled into oscillations.

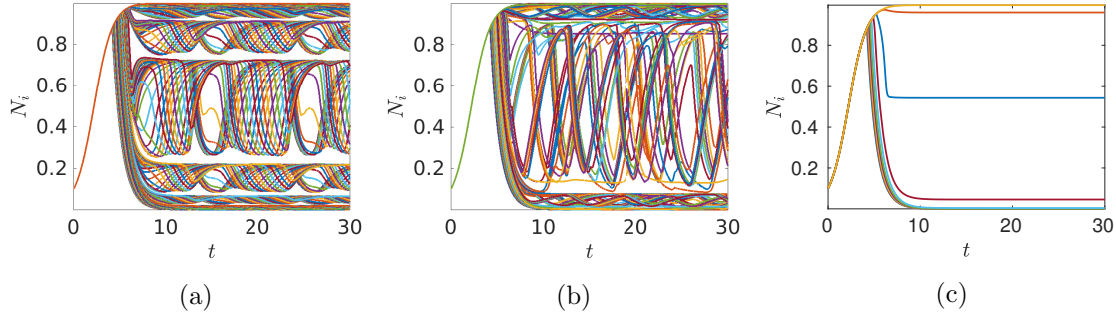


Figure 6: Nodal plots of cell densities for a lattice of size  $n = 25$ ,  $\delta = 10^{-3}$ ,  $p_l = 500$  with (a) no-flux conditions on the horizontal boundaries, (b) periodic conditions on these boundaries, and (c) the 1-D model.

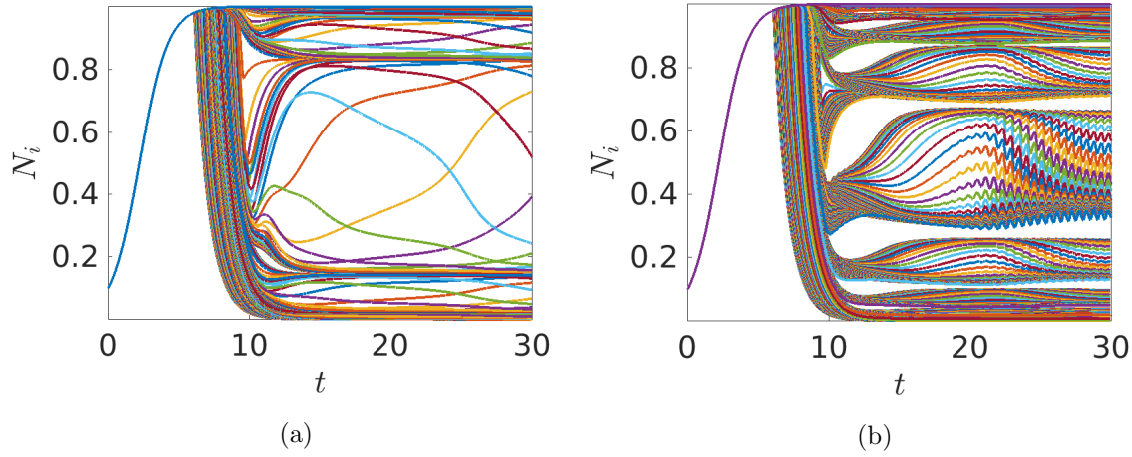


Figure 7: Plots of the cell density at each node for  $\delta = 10^{-4}$ ,  $p_l = 5,000$ , with (a)  $n = 50$ , and (b)  $n = 100$ .

of a small ( $n = 10$ ) lattice to a particular steady state. Then in Figures 10b through 10d we add increasing perturbations to a single node at the top-right of the lattice. We observe small excursions from the equilibrium for very small perturbations, larger excursions from equilibrium for larger perturbations, and finally a large enough perturbation induces a pulsing oscillation. This excitability is due to the nonlocal nature of the quasi-static fluid coupling, in that an increase in cell density at one node in the lattice affects the overall flow through the scaffold instantaneously and hence the pressure at every other node. This is particularly true for nodes that have high cell density as the nonlinearity in the relationship between pressure and cell densities amplifies the effect of large cell densities. In Section 5, we use numerical

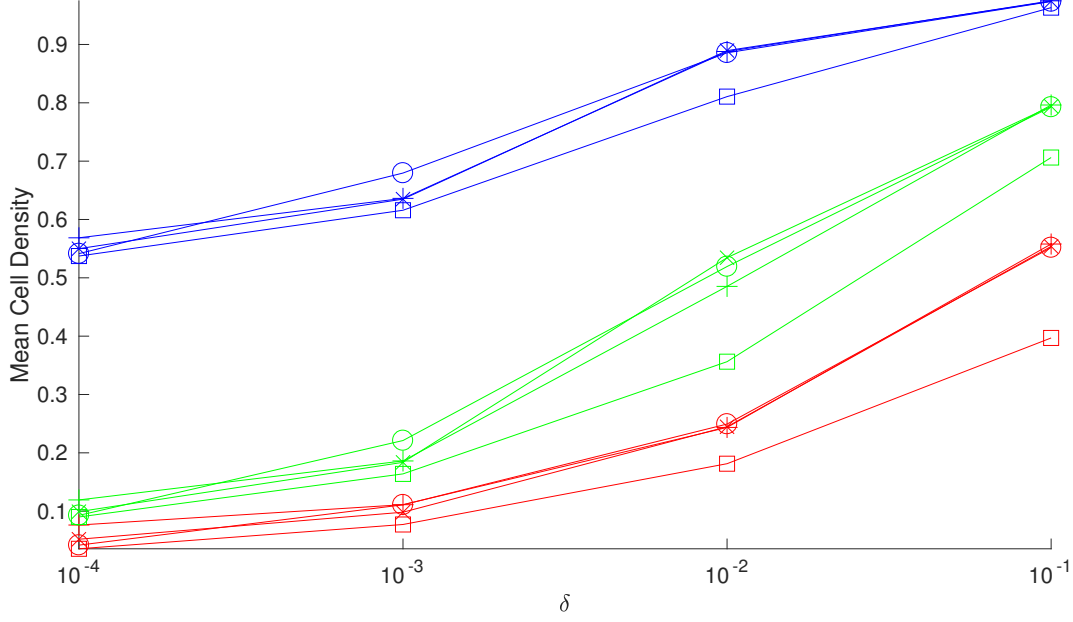


Figure 8: Mean cell density across several simulations of the lattice and the PDE models over four values of  $\delta$  averaged over the time from  $t = 20$  to  $t = 30$ . The symbols  $+$ ,  $\times$ ,  $\circ$ , and  $\square$  are for the lattice sizes  $n = 25, 50, 100$ , and the PDE respectively. The colors red, green, and blue correspond to  $p_l = 10p_c = 50, 500$ , and  $5000$ , respectively.

continuation to show the existence of locally stable steady states and pulsing oscillations for the same regions in parameter space, which helps to explain this behaviour as a large enough perturbation can move the state of the system between basins of attraction between these asymptotic behaviours.

The smoothing parameter  $g$  plays only a marginal role in these oscillations. The behaviours found in all of the simulations so far are qualitatively and quantitatively the same in the limit of  $g \rightarrow \infty$ . To check this, we replaced the functions  $F_1$  and  $F_2$  in Equations (4) with Heaviside step-functions, and obtained quantitatively comparable results. In the other direction, we set  $g = 1$  and repeated the simulation in Figure 4a to produce Figure 11, which appears to have only small differences in the initial transient leading up to the oscillation, and broadly the same behaviour. In contrast, the oscillations in Figures 5 and 6 were not present if  $g = 1$  for any parameters simulated, and instead steady state behaviour was obtained. This indicates that these non-vertically symmetric oscillations are related to sharp transitions between cell growth and death due to pressure. This also shows a robustness present in the symmetry-preserving oscillations that is not found in the more complicated behaviours.

We can modify our model to account for quiescent cell states, without growth or death, induced by high pressure that is not high enough to kill the cells. We plot an example of this in Figure 12. These figures are generated by adding a term  $z$  to the threshold inside of the function  $F_2$  from Equations (4), so that  $F_2(p_i) = (\frac{1}{2}) (\tanh[g(p_i + z - p_l)] + 1)$ . For

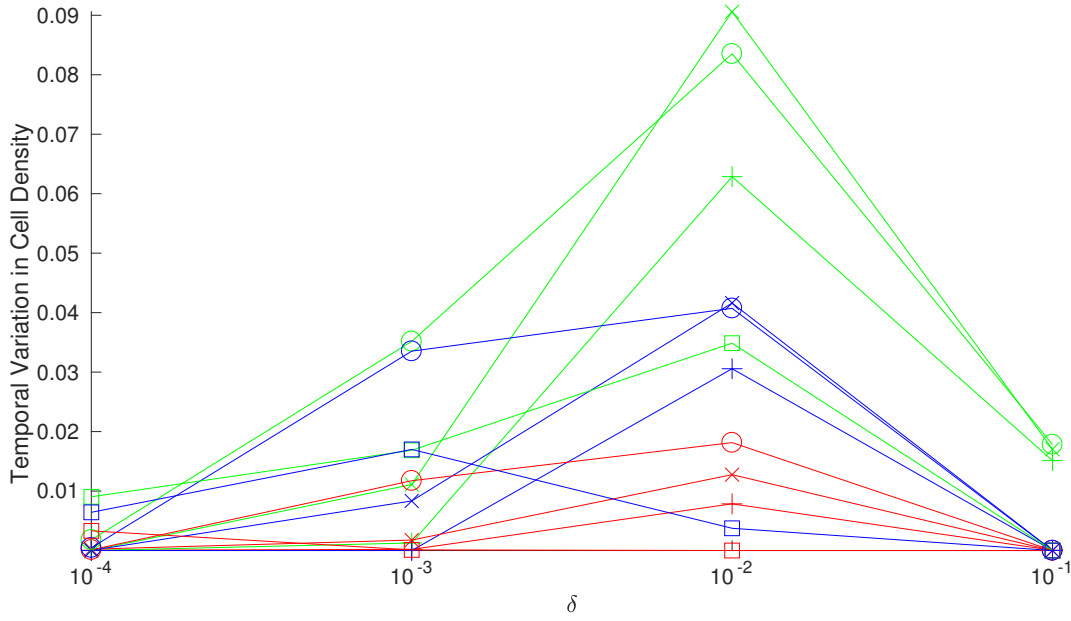


Figure 9: Variation in the mean cell density across several simulations of the lattice and the PDE models over four values of  $\delta$  averaged over the time from  $t = 20$  to  $t = 30$ . The symbols  $+$ ,  $\times$ ,  $\circ$ , and  $\square$  are for the lattice sizes  $n = 25, 50, 100$ , and the PDE respectively. The colors red, green, and blue correspond to  $p_l = 10p_c = 50, 500$ , and  $5000$ , respectively.

small values of  $z$  relative to  $p_l$  the dynamics are broadly similar; compare Figures 12a and 12b. For increasing values of  $z$ , the form of the oscillation changes, with increasing period as  $z$  increases, and eventually the oscillation appears to be damped out due to diffusion for a large enough quiescent regime, as in Figure 12f. Depending on the parameters we have found that the period of the oscillation can be extended from  $\approx 1$  time unit to greater than 3000 time units. Our numerical results suggest that capturing quiescent behaviour may have a comparable effect to smoothing the pressure forcing on the cells (e.g. decreasing the value of  $g$ ) in terms of asymptotic dynamics for small  $z$ , whereas large  $z$  tends to regularize the dynamics leading toward more steady state behaviours. We do not explore these variations further here.

Modulo differences in the constitutive relations, the behaviour of the PDE model and larger lattices is similar. This is expected due to the similarities between the lattice equations and a method-of-lines discretization of the PDE. In Section 5 we use simulations from a large subset of the feasible parameter space ( $\delta$ ,  $p_l$ , and  $p_c$ ) to understand typical behaviours of these models in general, and in particular provide evidence that smaller lattices have more complicated behaviours. Before demonstrating these results, we describe some asymptotic approaches that allow us to restrict our numerical efforts to specific parameter regimes.

**4. Asymptotic Solutions in the Large Diffusion Limit.** For large values of the diffusion  $\delta$ , solutions numerically approach an equilibrium with small variation between nodal values.



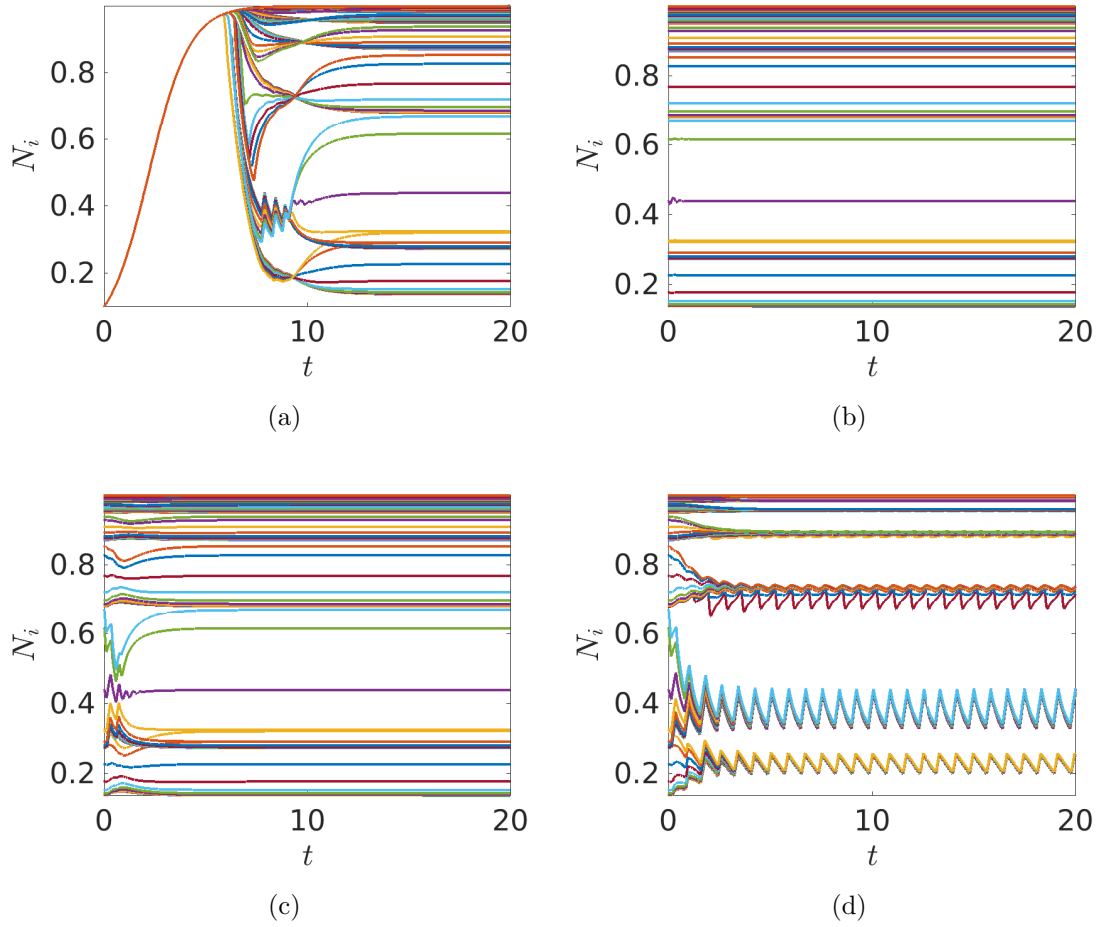


Figure 10: Excitable dynamics with  $n = 10$ ,  $p_l = 4000$ ,  $\delta = 10^{-2}$ . In (a) we show the trajectory from a uniform state to a nonuniform equilibrium at each node. In (b)-(d) we show how perturbations of the final state from node (a) evolve. These perturbations are to node  $N_{91}$  at the bottom right of the lattice, and of sizes  $10^{-5}$  in (b),  $3 \times 10^{-4}$  in (c) and  $4 \times 10^{-4}$  in (d).

Given this numerical evidence, we pursue an asymptotic solution for both models in this limit where  $1/\delta \ll 1$ . This asymptotic solution then allows us to quantitatively predict the solution structure for large values of  $\delta$ , bounding the region in parameter space that we explore in Section 5.

In all of the following, we simplify the pressure forcing terms. Letting  $g \rightarrow \infty$  our pressure functions become  $F_1(p_i) = H(p_l - p_i)$  and  $F_2(p_i) = H(p_i - p_l)$ , where  $H$  is the Heaviside step function. For convenience, we take  $H$  to be continuous on the right, so that  $\lim_{\varepsilon \rightarrow 0^+} H(\varepsilon) = H(0) \equiv 1$ .

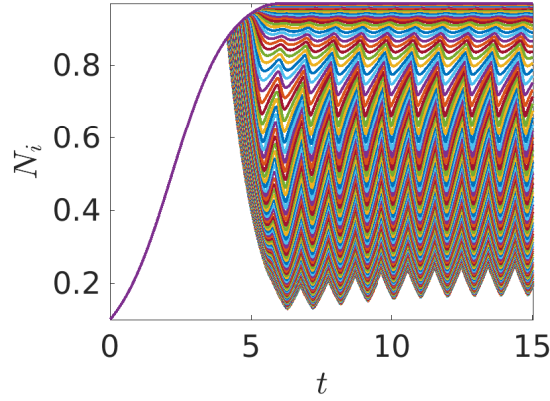


Figure 11: Time series of nodal values of the cell density for a lattice of size  $n = 100$ ,  $\delta = 10^{-2}$ ,  $p_l = 500$  with smoothed pressure forcing given by  $g = 1$ .

**4.1. Lattice Asymptotics.** We first consider solutions in the large diffusion limit for the lattice. We rewrite Equation (2) as,

$$(23) \quad \delta^{-1} \frac{dN_i}{dt} = \delta^{-1} (H(p_l - p_i)N_i(1 - N_i) - H(p_i - p_l)N_i) - n^2 \sum_{j=1}^{n^2} L_{ij}N_j.$$

We expand our variables as  $N_i = N_{0,i} + \delta^{-1}N_{1,i} + O(\delta^{-2})$  and  $p_i = p_{0,i} + \delta^{-1}p_{1,i} + O(\delta^{-2})$ . Substituting these expansions into Equation (23) and formally equating powers of  $\delta$  we find that the first order equation for the cell density  $N_{0,i}$  is,

$$(24) \quad 0 = -n^2 \sum_{j=1}^{n^2} L_{ij}N_{0,j}.$$

The graph Laplacian  $L$  has one zero eigenvalue with the corresponding eigenvector  $v = (1, 1, \dots, 1)^T$  [18]. Therefore, we know that the first order cell densities are all equal, that is  $N_{0,i} = N_0$  for some  $N_0$  for all  $i$ .

To find  $N_0$  we look at the second order problem,

$$(25) \quad \frac{dN_0}{dt} = (H(p_l - p_{0,i})N_0(1 - N_0) - H(p_{0,i} - p_l)N_0) - n^2 \sum_{j=1}^{n^2} L_{ij}N_{1,j}.$$

The pressure problem is independent of  $\delta$ , and as a spatially constant cell density  $N_0$  is vertically symmetric, we can use the solution in Equation (15) for the pressures which we rewrite as  $\hat{p}_{0,i}$ . Summing Equation (25) over  $i$  and noting that  $\sum_{i=1}^{n^2} L_{ij} = 0$  we find,

$$(26) \quad n \frac{dN_0}{dt} = \sum_{i=1}^{n^2} (H(p_l - \hat{p}_{0,i})N_0(1 - N_0) - H(\hat{p}_{0,i} - p_l)N_0).$$

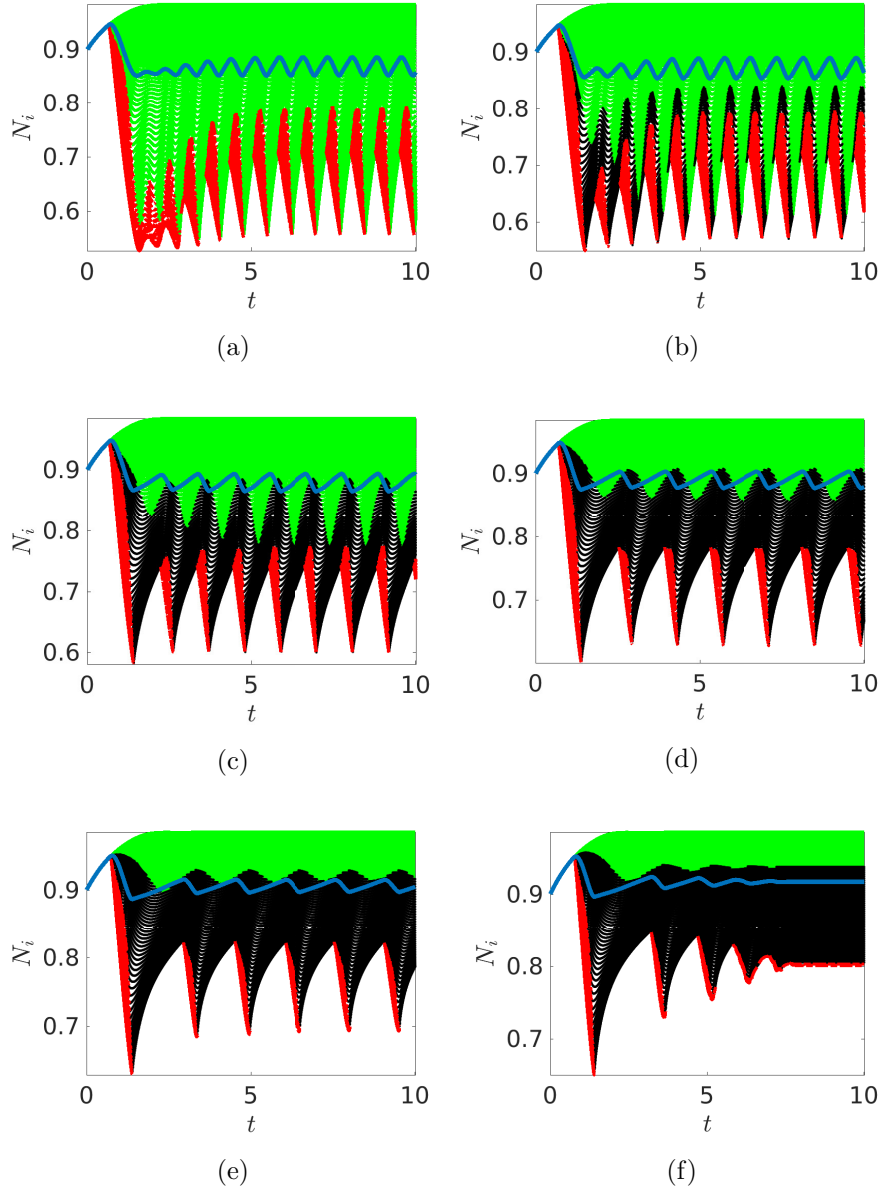


Figure 12: Time series of nodal values of the cell density for a 1-D lattice of size  $n = 100$ , with  $\delta = 0.05$  and  $p_l = 2000$ . In (a) we have no quiescent regime (e.g. cells go from growing to dying immediately as pressure is varied). We then increase the threshold in the function  $F_2$  by  $z = 10, 50, 100, 200$ , and  $300$  in each subsequent plot (b)-(f). Green nodes are growing ( $p_i < p_l$ ), red nodes are dying ( $p_i > p_l + z$ ) and black nodes are quiescent, only changing value due to diffusion ( $p_l < p_i < p_l + z$ ). We overlay the mean cell density in blue in each plot.

The vertically symmetric pressures  $\hat{p}_{0,i}$  are monotonically decreasing in  $i$  with  $\hat{p}_{0,n} = \frac{1}{n}$ . If  $\hat{p}_{0,1} < p_l$ , then equation (26) indicates that  $N_0 = 1$  is the only stable steady state, as  $H(\hat{p}_{0,i} - p_l) = 0$  for all  $i$ . If instead  $c < \frac{1}{n}$ , then  $N_0 = 0$  is the only stable steady state, as  $H(p_l - \hat{p}_{0,i}) = 0$  for all  $i$ . In all other cases, there exists an  $m = m(N_0)$  such that  $\hat{p}_{0,m} \geq p_l$  and  $\hat{p}_{0,m+1} < p_l$ . Then solutions of Equation (26) satisfy,

$$(27) \quad n \frac{dN_0}{dt} = (n - m(N_0))N_0(1 - N_0) - m(N_0)N_0.$$

We can solve for  $m(N_0)$  as a function of our cell density  $N_0$ . Using Equation (15) we find,

$$(28) \quad m(N_0) = [n - R^4(N_0, N_0)(p_l n - 1)]^+ = [n - (1 - \rho N_0)^4(p_l n - 1)]^+,$$

where  $[f]^+ = \max(f, 0)$  is the positive part of the function  $f$ . This is necessary as for small  $N_0$ , corresponding to  $p_i < p_l$  for all  $i$ , the solution for  $m(N_0)$  is negative. Equations (27) and (28) represent a single scalar first-order ordinary differential equation, compared with the original  $n^2$  differential equations (2) and  $n^2$  algebraic equations (1), although our scalar equation is not smooth due to the positivity assumption on  $m(N_0)$ .

We look for a steady state  $N_0^* > 0$  to Equation (27), assuming that  $m(N_0^*) > 0$ , which follows from the assumptions on the ranges of  $p_l$  discussed at the beginning of section 3. Substituting (28) into Equation (27), dividing by  $N_0$ , and setting the time derivative equal to zero, we have that  $N_0^*$  should satisfy,

$$(29) \quad 0 = R^4(N_0^*, N_0^*)(p_l n - 1)(2 - N_0^*) - n = (1 - \rho N_0^*)^4(p_l n - 1)(2 - N_0^*) - n,$$

which is a quintic polynomial in  $N_0^*$ . We now show that equation (29) has at most one unique real root in the interval  $(0, 1)$ . Let  $\tilde{N} = R(N_0^*, N_0^*) = 1 - \rho N_0^*$ . Then since  $0 < \rho < 1$  and assuming  $0 \leq N_0^* \leq 1$  we have that  $0 \leq \tilde{N} \leq 1$ . We rewrite equation (29) as,

$$(30) \quad 0 = \tilde{N}^4(p_l n - 1) \left( 2 - \frac{1}{\rho} + \frac{\tilde{N}}{\rho} \right) - n = \tilde{N}^5 \frac{(p_l n - 1)}{\rho} + \tilde{N}^4(p_l n - 1) \left( 2 - \frac{1}{\rho} \right) - n,$$

which has only one sign change in its coefficients (as  $p_l > 1/n$  by assumption). So by Descartes' rule of signs, equation (30) has at most one positive root, implying uniqueness of the positive real root  $N_0^*$  of equation (29) in the interval  $(0, 1)$ .

The uniqueness of the root  $N_0^*$  found above implies that there are three possible steady states of equation (27) in the interval  $[0, 1]$ . If  $m(0) = 0$ , then  $N_0 = 0$  is a steady state solution. Similarly if  $m(1) = 0$ , then  $N_0 = 1$  is a steady state. Finally, if  $m(N_0^*) > 0$ , then the argument above shows the existence of a unique steady state  $N_0^* \in (0, 1)$ . We now argue by monotonicity that this root is globally attractive for initial data in the interval  $[0, 1]$ , and construct solutions to equation (27).

The function  $m(N_0)$  given by (28) is monotonically increasing in  $N_0$ . So there is a unique value  $\hat{N}_0$  such that  $m(\hat{N}_0) = 0$ . From this we compute that

$$(31) \quad \hat{N}_0 = \frac{1 - \left( \frac{n}{p_l n - 1} \right)^{\frac{1}{4}}}{\rho},$$

which we note is within the interval  $[0, 1]$  given the bounds of  $p_l$  and  $\rho$  discussed in Section 3. By monotonicity, we have that  $m(N_0) \geq 0$  for all  $N_0 \in [\hat{N}_0, 1]$ . So  $m(0) = 0$  and  $m(1) > 0$ , which allows us to verify that  $N_0 = 0$  is an unstable steady state and  $N_0 = 1$  is not a steady state solution. Simple substitution shows that  $N'_0(t) < 0$  when  $N_0 = 1$ , and so continuous solutions to equation (27) do not leave the interval  $[0, 1]$ , which is consistent with the boundedness of solutions to the full system shown in Section 2.2. We can further bound solutions by noting that for  $m(N_0) = 0$ , the right side of (27) is positive, so solutions approach  $\hat{N}_0$ . Similarly, for all  $\epsilon > 0$  sufficiently small, the right side of (27) is positive for  $N_0 = \hat{N}_0 + \epsilon$ . So the region  $(\hat{N}_0, 1)$  absorbs solutions with initial data  $N_0(0) \in (0, 1]$ , and hence we must have that  $N_0^* \in (\hat{N}_0, 1)$ .

We can solve equation (27) by considering the cases when  $N_0(0) < \hat{N}_0$  and  $N_0(0) > \hat{N}_0$  separately. We first assume that  $N_0(0) \in (0, \hat{N}_0)$ . Then, by the monotonicity of  $m$ , we have that in some finite time  $t_s$  our solution changes from one solution branch to another corresponding to when  $N_0(t_s) = \hat{N}_0$ . So we write

$$(32) \quad \frac{dN_0}{dt} = \begin{cases} N_0(1 - N_0) - N_0, & t \leq t_s, \\ (1 - \rho N_0)^4 (p_l - \frac{1}{n}) N_0(2 - N_0) - N_0, & t > t_s. \end{cases}$$

The solution to equation (32) for  $t \leq t_s$  is a logistic function,

$$(33) \quad N_0(t) = \frac{N_0(0)e^t}{N_0(0)(e^t - 1) + 1}, \quad t \leq t_s,$$

which we can use to compute  $t_s$ . We set  $N_0(t_s) = \hat{N}_0$  and use equations (31) and (33) to find

$$(34) \quad t_s = \ln \left( \frac{(1 - N_0(0))(1 - (\frac{n}{np_l - 1})^{\frac{1}{4}})}{N_0(0) \left( (\frac{n}{np_l - 1})^{\frac{1}{4}} + \rho - 1 \right)} \right),$$

We consider equation (32) for  $t > t_s$ . This equation has a sixth-order polynomial nonlinearity, and we are not aware of a method to explicitly integrate it. We know by the boundedness of  $N_0(t)$ , however, that  $N_0(t_s)$  is close in a nondimensional sense to our equilibrium value  $N_0^*$  for any initial mean cell density  $N_0(0)$ . So we expect approximately exponential convergence to  $N_0^*$  for  $t > t_s$ . We substitute the ansatz

$$(35) \quad N_0(t) = N_0^* + Ae^{-r(t-t_s)}, \quad t > t_s,$$

for  $|A| < 1$  into equation (32), and take the Taylor series of the right hand side about  $A = 0$  to find

$$(36) \quad -rAe^{-r(t-t_s)} = (1 - \rho N_0^*)^4 \left( p_l - \frac{1}{n} \right) N_0^*(2 - N_0^*) - N_0^* \\ + \left\{ \left( p_l - \frac{1}{n} \right) (2(1 - \rho N_0^*)^4 (1 - 1N_0^*) - 4(1 - \rho N_0^*)^3 N_0^*(2 - N_0^*)\rho) - 1 \right\} Ae^{-r(t-t_s)} + O(A^2).$$

The leading order term in  $A$  on the right hand side of equation (36) is zero, as  $N_0^*$  is the solution to equation (29). So assuming  $A$  is small, we have

$$(37) \quad r \sim \left( p_l - \frac{1}{n} \right) (4(1 - \rho N_0^*)^3 N_0^* (2 - N_0^*) \rho - 2(1 - \rho N_0^*)^4 (1 - N_0^*)) + 1.$$

In order to match our solution for  $t \leq t_s$ , we take  $A = N_0(t_s) - N_0^*$  where  $N_0(t_s)$  is the solution from equation (33) evaluated at  $t = t_s$ . Our asymptotic solution can then be written as

$$(38) \quad N_0(t) = \begin{cases} \frac{N_0(0)e^t}{N_0(0)(e^t-1)+1} & t \leq t_s, \\ N_0^* + \left( \frac{N_0(0)e^{t_s}}{N_0(0)(e^{t_s}-1)+1} - N_0^* \right) e^{-r(t-t_s)}, & t > t_s, \end{cases}$$

where  $t_s$  is defined by equation (34) and  $r$  by equation (37).

Next we consider the case that  $N_0(0) > \tilde{N}_0$ . As  $m(N_0(0)) > 0$ , we can use the above asymptotic method to find an exponential asymptotic solution of the form given by equation (35) as before. Matching the solution to the initial data gives that  $A = N_0(0) - N_0^*$ . So the solution in this case is

$$(39) \quad N_0(t) = N_0^* + (N_0(0) - N_0^*)e^{-rt},$$

with  $r$  given by equation (37).

The solution given by equation (38) describes a period of logistic cell growth, followed by an exponentially fast convergence to a steady state, with the time between these periods and parameters in the solution determined by the initial mean cell density  $N_0(0)$  as well as parameters from the full problem. If the initial mean cell density is high enough to immediately cause cells to die due to pressure, then equation (39) describes the exponential convergence to a steady state in this case. These analytical solutions also match numerical solutions of (27) extremely well. In Figure 13 we demonstrate this. In the worst case of  $N_0(0) = 0.9$  and  $p_l = 10$ , where there is no logistic growth, we note that the analytical solution is still quite close to the numerical solution despite the asymptotic parameter  $A = 0.45$  being large in this case. We suspect this is due in part to solutions being bounded in  $[0, 1]$ , so that we always have  $|A| < 1$ , along with the existence of a unique stable steady state to equation (27).

We compare the asymptotic solution (38) for the cell density  $N_0$  against the mean cell density for the full two-dimensional problem (1)-(4) for various values of  $\delta$  in Figure 14. For small values of  $\delta$ , the oscillations in cell density have an overall effect on the mean cell density such that our asymptotic solution over-predicts the oscillatory mean cell density. Increasing  $\delta$ , we see a relatively fast convergence to the asymptotic solution for the mean cell density  $N_0$ . Comparable results hold for different values of  $p_l$  and  $n$ , and for the solution given by equation (39).

In Figure 15 we plot three values of mean cell densities for simulated solutions of equations (1)-(4) for a lattice with  $n = 10$ , along with corresponding mean cell densities computed from equations (29). The large  $\delta$  asymptotic solution  $N_0$  accurately predicts the mean cell density for  $\delta \approx 1$  for all values of  $p_l$ , and for smaller values of  $\delta$  for larger values of  $p_l$ . For smaller values of  $\delta$ , the variation from the asymptotic solution is due to significant spatial variation in the cell density  $N_i$ . The sharp points in the plots are due to changes in the number of

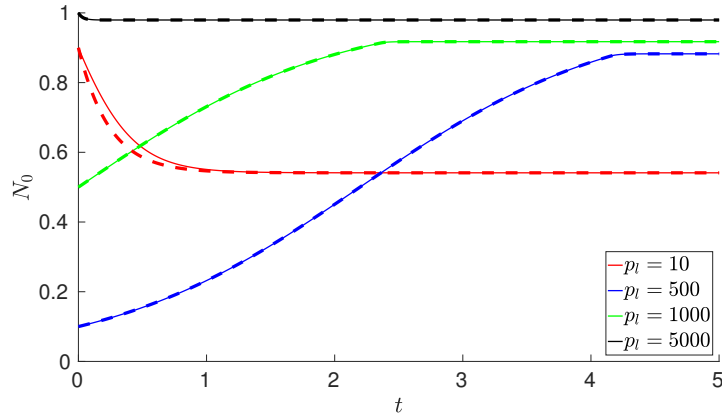


Figure 13: Plots of mean cell density computed from simulations of equations (27)-(28) as solid lines, as well as the asymptotic solutions (38)-(39) as dashed lines, for  $n = 10$  and different initial mean cell densities  $N_0(0)$  and thresholds  $p_l$ .

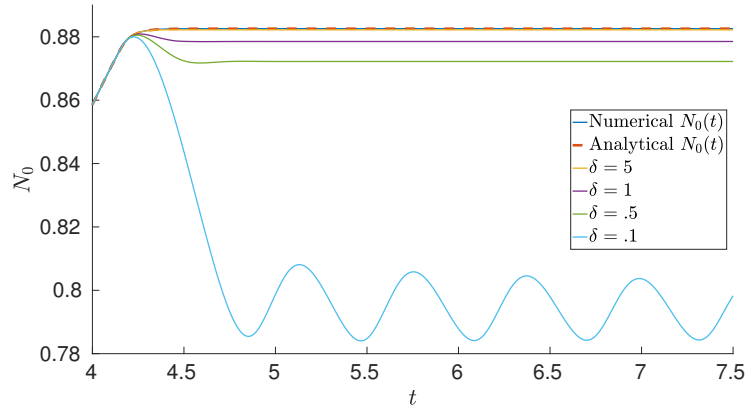


Figure 14: Plots of mean cell density computed from numerical solutions of equations (27)-(28), analytical solutions given by (38), and simulations of the full two-dimensional model (1)-(4) for  $n = 100$ ,  $p_l = 500$ , and  $\delta = 0.1, 0.5, 1$ , and  $5$ .

grid points that are growing or dying, rather than coarse sampling. For some values of  $\delta$  the numerical solutions were oscillatory, and this behaviour undoubtedly affects the mean cell density computed as in Figure 14.

**4.2. PDE Asymptotics.** As in Section 4.1, we divide equation (6) by  $\delta$  and expand our variables as  $N = N_0 + \delta^{-1}N_1 + O(\delta^{-2})$  and  $p = p_0 + \delta^{-1}p_1 + O(\delta^{-2})$ . At first order we have

$$(40) \quad \nabla^2 N_0 = 0,$$



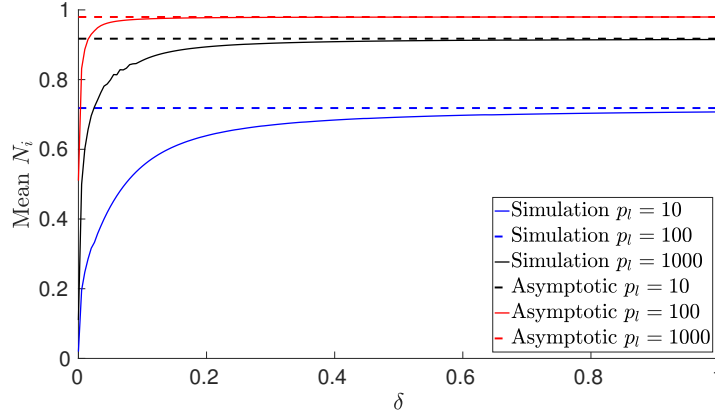


Figure 15: Plots of mean cell density for lattices at three different values of the threshold  $p_l$  against the predicted steady state solution from equation (29).

which, along with the boundary condition in equations (10), shows that  $N_0$  is constant throughout the domain (e.g. by the Maximum Principle). To find its value we look at the second order problem,

$$(41) \quad \frac{\partial N_0}{\partial t} = H(p_c - p_0)N_0(1 - N_0) - H(p_0 - p_c)N_0 + \nabla^2 N_1,$$

where we have again considered Heaviside functions in the limit of  $g \rightarrow \infty$  for  $F_1$  and  $F_2$ .

Integrating equation (41) over the domain we find,

$$(42) \quad \frac{\partial N_0}{\partial t} = \int_0^1 H(p_c - p_0(x))N_0(1 - N_0) - H(p_0(x) - p_c)N_0 dx,$$

where we have used the boundary conditions in equation (10) to drop the  $N_1$  term.

As  $N_0$  is spatially constant, we use equation (19) to write  $p_0$  in terms of  $N_0$  and  $x$ . We have that  $p_0(x) = (1 - x)/k(N_0)$  which is monotonically decreasing in  $x$ . There must exist a point  $x^*(N_0)$  such that for all  $x \leq x^*(N_0)$ ,  $p_0(x) \geq p_c$ , and for all  $x > x^*(N_0)$ ,  $p_0(x) < p_c$ . So we have,

$$(43) \quad \frac{\partial N_0}{\partial t} = (1 - x^*(N_0))N_0(1 - N_0) - x^*(N_0)N_0,$$

where  $x^*(N_0) = [1 - p_c k(N_0)]^+ = [1 - p_c(1 - \rho N_0)^3]^+$ , where again the positive part must be taken to avoid a negative value of  $x^*(N_0)$  for small  $N_0$ . We have reduced a system of two partial differential equations in equations (5)-(6) to equation (43) which is an ordinary differential equation, although again there is a nonsmooth component due to  $x^*(N_0)$ . At steady state, the solution  $N_0^*$  must satisfy,

$$(44) \quad 0 = p_c k(N_0^*)(2 - N_0^*) - 1,$$

where we are neglecting the unstable steady state  $N_0 = 0$ . This is a quartic equation for  $N_0$  which can be solved numerically. Up to constitutive differences giving different exponents between  $k(N_0)$  and  $R^{-4}(N_0)$ , it can also be seen as the limit of equation (29) as  $n \rightarrow \infty$ .

As in equation (29), the solution  $N_0^*$  to equation (44) can be shown to have a unique solution in the interval  $(0, 1)$ . Let  $\tilde{N} = 1 - \rho N_0^*$ . Then we have  $0 < \tilde{N} < 1$  and  $\tilde{N}^4 + (2\rho - 1)\tilde{N}^3 - \rho/p_c = 0$ , which can have at most one sign change, and hence a maximum of one positive root of  $\tilde{N}$ . A negative root corresponds to  $N_0^* > 1$ , which is prohibited by the dynamics of the cell equation.

Following the procedure in Section 4.1 to derive equation (38), we can solve equation (43). If we assume that  $N_0(0) < \hat{N}_0$  where the value  $\hat{N}_0$  satisfies  $x^*(\hat{N}_0) = 0$ , we find the solution takes the form

$$(45) \quad N_0(t) = \begin{cases} \frac{N_0(0)e^t}{N_0(0)(e^t-1)+1}, & t \leq t_c, \\ N_0^* + \left( \frac{N_0(0)e^{t_c}}{N_0(0)(e^{t_c}-1)+1} - N_0^* \right) e^{-r_c(t-t_c)}, & t > t_c, \end{cases}$$

where  $N_0(0)$  is the initial mean cell density,  $N_0^*$  is the unique root of equation (44), the switching time  $t_c$  is given by

$$(46) \quad t_c = \ln \left( \frac{(1 - N_0(0))(1 - (p_c^{\frac{1}{3}} - 1))}{N_0(0)(1 - (1 - \rho)p_c^{\frac{1}{3}})} \right),$$

and  $r_c$  is given by

$$(47) \quad r_c = p_c(3(1 - \rho N_0^*)^2 N_0^*(2 - N_0^*)\rho - 2(1 - \rho N_0^*)^3(1 - N_0^*)) + 1.$$

Similarly, if we assume that the initial cell density satisfies  $N_0(0) > \hat{N}_0$ , then we find the following form for the solution,

$$(48) \quad N_0(t) = N_0^* + (N_0(0) - N_0^*)e^{-r_c t}.$$

The solution given by equation (45) is analogous to the lattice asymptotic solution (38), with different values of the switching time  $t_c$  and exponential convergence rate  $r_c$ . Likewise the exponential solution (48) is comparable to the lattice solution (39). In Figure (16) we compare the analytical and numerical solutions to equation (43). The worst case behaviour, shown in red, corresponds to the asymptotic parameter  $N_0^* - N_0(t_c) = 0.5$ , so it is not surprising that there is a transient discrepancy in this case.

We compare this solution for the cell density  $N_0$  against the mean cell density for the full two-dimensional problem (5)-(10) for various values of  $\delta$  in Figure 17. For small values of  $\delta$ , as in the lattice case, there is some discrepancy with our asymptotics due to spatial structure in the solutions. As we increase  $\delta$ , however, we see a relatively fast convergence to the asymptotic solution for the mean cell density  $N_0$ . Comparable results hold for different values of  $p_c$ , and we suspect the range of  $\delta$  for which the asymptotic value of  $N_0$  is a good approximation is larger for the continuous model than for the lattice. To see this, compare Figures 14 and 17, and note the ranges on the axes.

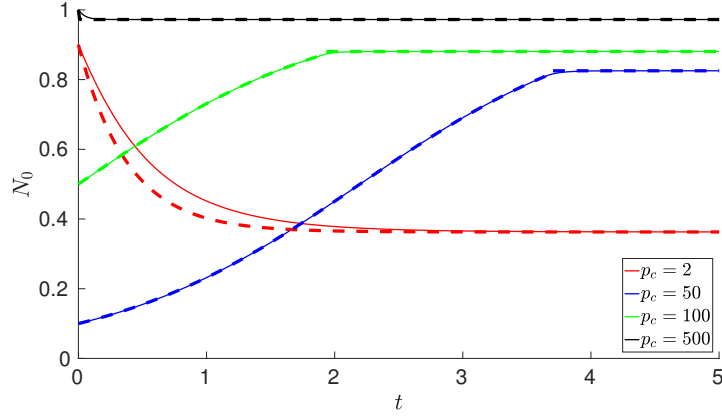


Figure 16: Plots of mean cell density computed from simulations of equation (43) as solid lines, as well as the asymptotic solutions, (45) for increasing curves and (48) for decreasing curves, as dashed lines for different initial mean cell densities  $N_0(0)$  and thresholds  $p_l$ .

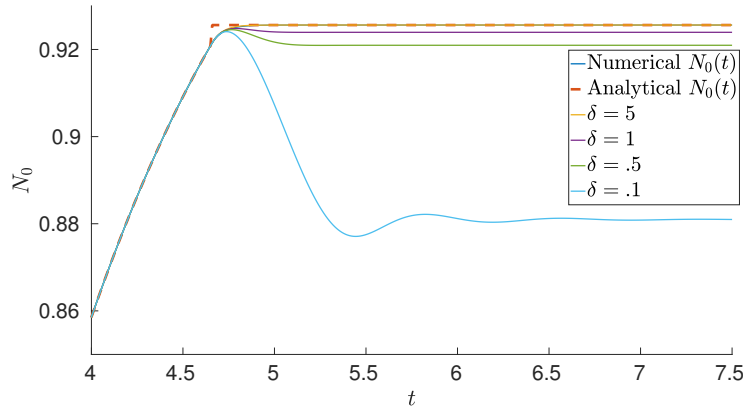


Figure 17: Plots of mean cell density computed from numerical solutions of equations (43), analytical solutions given by (45), and simulations of the full two-dimensional model (5)-(10) for  $p_c = 200$ , and  $\delta = 0.1, 0.5, 1$ , and  $5$ .

**5. Bifurcations in Small and Large Lattices.** We now consider the qualitative behaviours observed in Section 3 from the perspective of bifurcations and coarse classifications of the parameter space. Motivated by the simple dynamics of the asymptotic results in 4, we concentrate on changes with respect to small values of  $\delta$ . For the pressure thresholds  $p_l$  and  $p_c$ , we know that these must be bounded as described in Section 3 to obtain nontrivial dynamics.

We first examine a low-dimensional ( $n = 4$ ) lattice model, and numerically continue steady state solutions. We track their stability by evaluating the Jacobian of the system and

computing its eigenvalues [21]. We use natural parameter continuation and manually switch branches, as we are only interested in solution branches that are stable in some region of the parameter space. Equations (1) can be viewed as a weighted graph Laplace equation, and so can be inverted numerically to find the pressures as functions of the cell density. Therefore, in computing Jacobians we only consider the  $n^2 \times n^2$  matrix corresponding to the Jacobian of equations (2) with  $p_i$  a function of  $N_1, \dots, N_{n^2}$  for all  $i$ . We denote the  $i$ th eigenvalue of the Jacobian evaluated along a branch of steady states by  $\sigma_i$ . We fix the value of  $p_l = 15$  and use  $\delta$  as a continuation parameter to demonstrate some of the behaviours found in our continuation studies.

In Figure 18, we plot the value of  $N_1$  corresponding to three steady state solution branches over varying diffusion  $\delta$ . The solid lines are steady states with all eigenvalues having negative real part,  $\max_i \Re(\sigma_i) < 0$ , and hence are locally linearly stable. The dashed lines have at least one eigenvalue with positive real part, and so are linearly unstable. Around  $\delta \approx 0.08$  (point A), the vertically symmetric state (black line) loses stability. There is a nearby oscillating solution, which has the same non-vertically symmetric character as the solution plotted in Figure 5. We plot the envelope of this oscillation in green corresponding to the maximum and minimum values that  $N_1$  takes during a period. For larger values of diffusion the oscillation is no longer observable and we suspect it becomes unstable around  $\delta \approx 0.47$  (point C'). As the amplitude of the oscillation is small when it first appears, we plot the two eigenvalues with largest real part in Figure 19, and show that at the point where the steady state loses stability, the eigenvalues cross the imaginary axis in a conjugate pair (e.g.  $\Im(\sigma_i) \neq 0$  for the two  $\sigma_i$  with largest real part). Since the oscillatory solution immediately beyond this loss of stability is numerically stable and its amplitude is small for  $\delta$  near the bifurcation point, we conjecture that this is a supercritical Hopf bifurcation giving rise to the stable limit cycle that we observe.

For  $\delta \approx 1.5$  (point D), two solution branches emerge from the vertically symmetric branch as it loses stability (for decreasing  $\delta$ ). These non-vertically symmetric solutions are reflected copies of one another, as is typical in a pitchfork bifurcation due to a reflection symmetry. We plot the eigenvalues of these continued branches in Figure 20 showing evidence that this is a pitchfork bifurcation (note that eigenvalues cross the imaginary axis with zero imaginary part). We plot cell densities at every lattice node in the insets of Figure 18 of all three steady state branches at the point  $\delta = 0.5$ . Note that the symmetric branch is unstable for this value of  $\delta$ . These non-symmetric branches both lose stability at  $\delta \approx 0.46$  (point C), again in what appears to be a Hopf bifurcation, as the eigenvalues with the largest real part again cross the imaginary axis in Figure 20. In this case, however, there is no small amplitude *stable* limit cycle, and instead solutions are attracted to the limit cycle previously generated, which has a large amplitude at this point. We conjecture that an unstable limit cycle exists to the right of the bifurcation point, between C and C', and that this may be what induces the loss of stability for the stable limit cycle, but we do not pursue these claims here. Lastly, we see that around  $\delta \approx 0.4$  (point B) the solution branches again merge, and the eigenvalues shown in Figure 20 have the same structure for the rest of the continued solution. While we have only shown plots for  $N_1$ , plots for all  $N_i$  show that these behaviours are qualitatively consistent across all states, and hence these branches, their stability, and the merging of branches are captured by Figure 18.

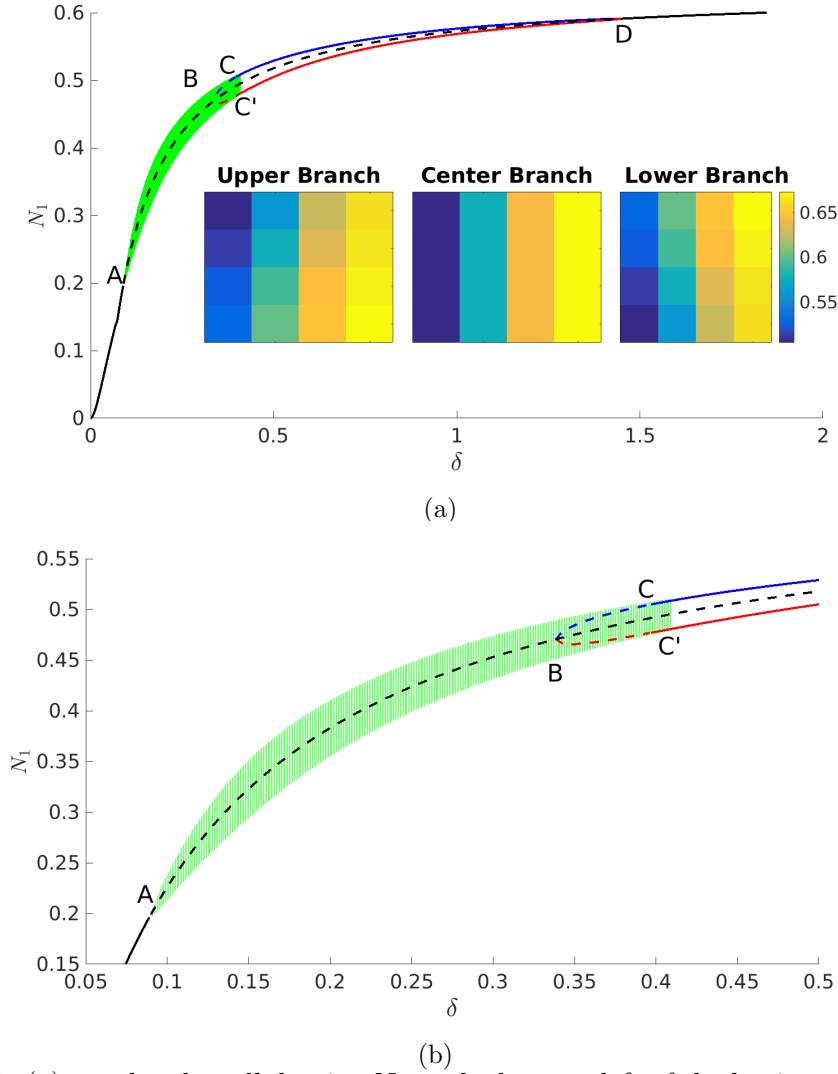


Figure 18: In (a) we plot the cell density  $N_1$  at the bottom-left of the lattice corresponding to three steady state branches found via numerical continuation. Solid lines correspond to locally stable steady states, dashed lines to unstable steady states, and the green lines represent an envelope of oscillations about the steady state solutions. The insets show cell density plots across the lattice at  $\delta = 0.5$ . For this case,  $p_l = 15$  and  $\rho = 0.9$ . The plot in (b) is a closer look at the oscillatory regime.

The results in Figures 18-20 suggest the existence of Hopf and pitchfork bifurcations, alongside multiple (non-vertically symmetric) steady states, and oscillatory behaviour in the 2-D lattice with  $n = 4$ . We did not observe any pulsing oscillations as in Figure 3. We briefly summarize results for other values of  $n$ . For  $n = 2$  and  $n = 3$  we only observed vertically symmetric steady states for a large region of parameter space. Similar behaviours

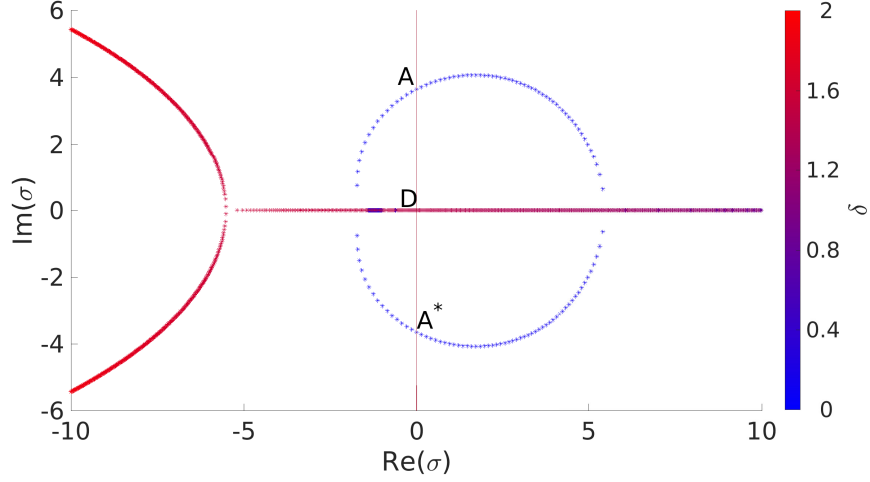


Figure 19: Plots of the two largest real part eigenvalues  $\sigma_i$  of the Jacobian evaluated at the vertically symmetric branch, colored according to the value of  $\delta$ . Note that after the blue pair of eigenvalues crosses the imaginary axis at A (with a complex conjugate eigenvalue at  $A^*$ ), where  $\Re(\sigma) = 0$ , the imaginary part decreases until the eigenvalues lie on the real axis, from which they move to the right as  $\delta$  increases, and eventually back to the left for larger  $\delta$ . The first crossing corresponds to a Hopf bifurcation, and the second, at point D, to a pitchfork bifurcation where the center branch again gains stability.

to  $n = 4$  (non-symmetric steady states and oscillations) were observed for  $n = 5, 6$ . For  $n = 7$ , the 2-D lattice had both vertically-symmetric pulsing oscillations, as in Figure 3 and the non-vertically symmetric oscillations described above. For the 1-D reduced model, we only observed steady state behaviour for  $n \leq 6$ , and oscillations along with steady states for  $n \geq 7$ . For parameter values where a pulsing oscillation exists but a non-vertically symmetric one does not, the vertically-symmetric steady state remains locally stable. This is true for both the 2-D and the 1-D models, and so the 1-D model exhibits a locally stable steady state solution for every parameter combination we simulated. This provides an explanation for the excitable behaviour in Figure 10, as the perturbations needed to be sufficiently large to move out of the basin of attraction of the locally stable steady state.

Even for small lattices, a complete classification of the phase space across a range of parameters is not tractable. Instead we now consider larger lattices and classify behaviours broadly as oscillatory or steady-state, and record properties of solutions. The results from Section 4 suggest that for large values of diffusion the cell density is approximated accurately by a spatially constant solution. For this reason we choose to do parameter sweeps between  $\delta = 0.001$  and  $\delta = 0.1$  to capture non-steady state behaviour in the models in a range where this approximation breaks down. We compute bifurcation plots in  $(\delta, p_l)$  and  $(\delta, p_c)$  in the following way. We first discretize the parameter space, and numerically simulate the governing equations at each discrete point for a sufficiently long period of time (we chose this time to be  $t = 40$ ), and then truncated our simulation to analyze only the last 10 units of time. For each

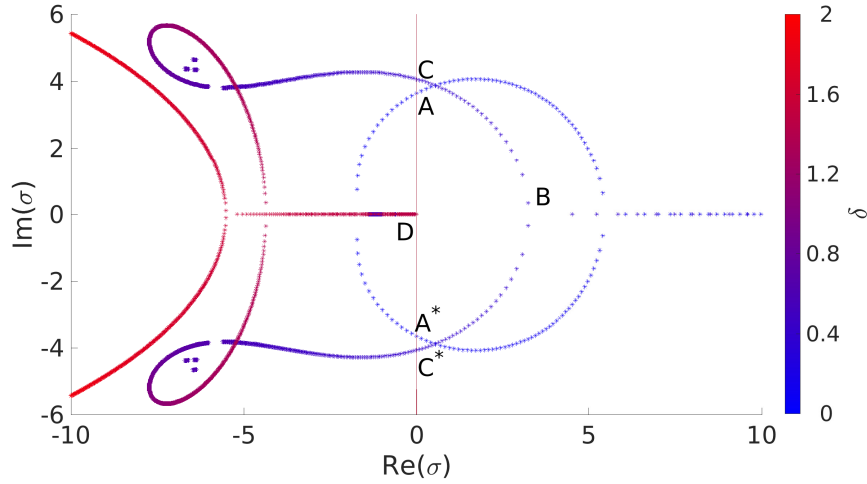


Figure 20: Plots of the two largest real part eigenvalues  $\sigma_i$  of the Jacobian evaluated at the upper branch, colored according to the value of  $\delta$ . Note that the eigenvalues along the lower branch are precisely the same for small  $\delta$ . For  $\delta \lesssim 0.4$  the eigenvalues follow the same trajectory as in Figure 19, undergoing a Hopf Bifurcation at A (with complex conjugate  $A^*$ ), but rather than returning along the real axis they develop a complex conjugate pair at B, and cross the imaginary axis in a pair at C and  $C^*$ . They approach the origin along the real axis at D, but remain in the left hand side of the plane, as this solution branch merges with the vertically-symmetric branch which gains stability at this point.

node, or in the case of the PDE for each interpolated discretized element, we compute the largest and smallest values this node takes in the truncated time series to compute a nodal oscillation amplitude.

In Figure 21 we plot the maximal amplitude of these nodal oscillations in the lattice. In Figure 22 we plot the frequency of nodal oscillations computed using the Fast-Fourier Transform of these truncated time series, and in Figure 23 we plot the mean cell density, where the mean is both in space and over the last 10 time units. We plot corresponding PDE bifurcation diagrams in Figure 24. For most of these simulations we took the diffusion to vary in steps of 0.001. For most of the lattice simulations we took the threshold parameter from  $p_l = 100$  to  $p_l = 10000$  in increments of 100. For the 1-D PDE simulations we took the threshold parameter from  $p_c = 10$  to  $p_c = 1000$  in increments of 10. Finally, for the 2-D  $n = 50$  bifurcation plot we used coarser sampling taking steps of 0.005 in  $\delta$  and 500 in  $p_l$ , and for the 2-D PDE and  $n = 100$  lattice we took steps of 0.01 in  $\delta$ , 100 in  $p_c$ , and 1000 in  $p_l$  respectively.

The larger lattices and the PDE appear to have a dominant oscillatory region for small  $\delta$  or small  $p_l$ . This corresponds to a parameter region where the mean cell density is significantly below the carrying capacity, and we conjecture that this is the criterion necessary for pulsing oscillations—that there is sufficient variation in cell density due either to small values of the diffusion or small pressure thresholds. The 2-D lattices, and especially the smaller ones,



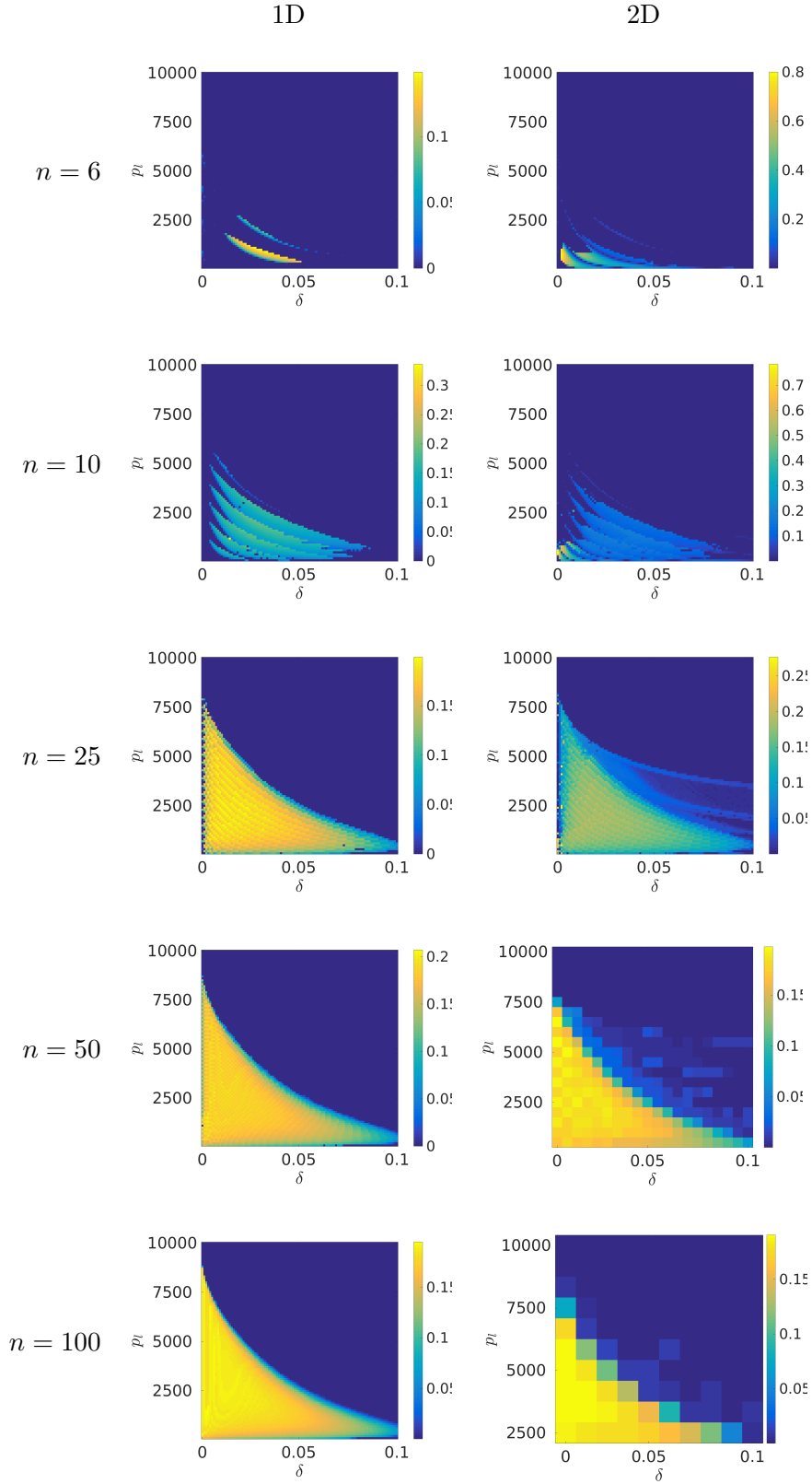


Figure 21: Amplitude of the maximal nodal oscillation after  $t = 40$  time units for different lattice sizes and dimensions over  $\delta$  and  $p_l$ .

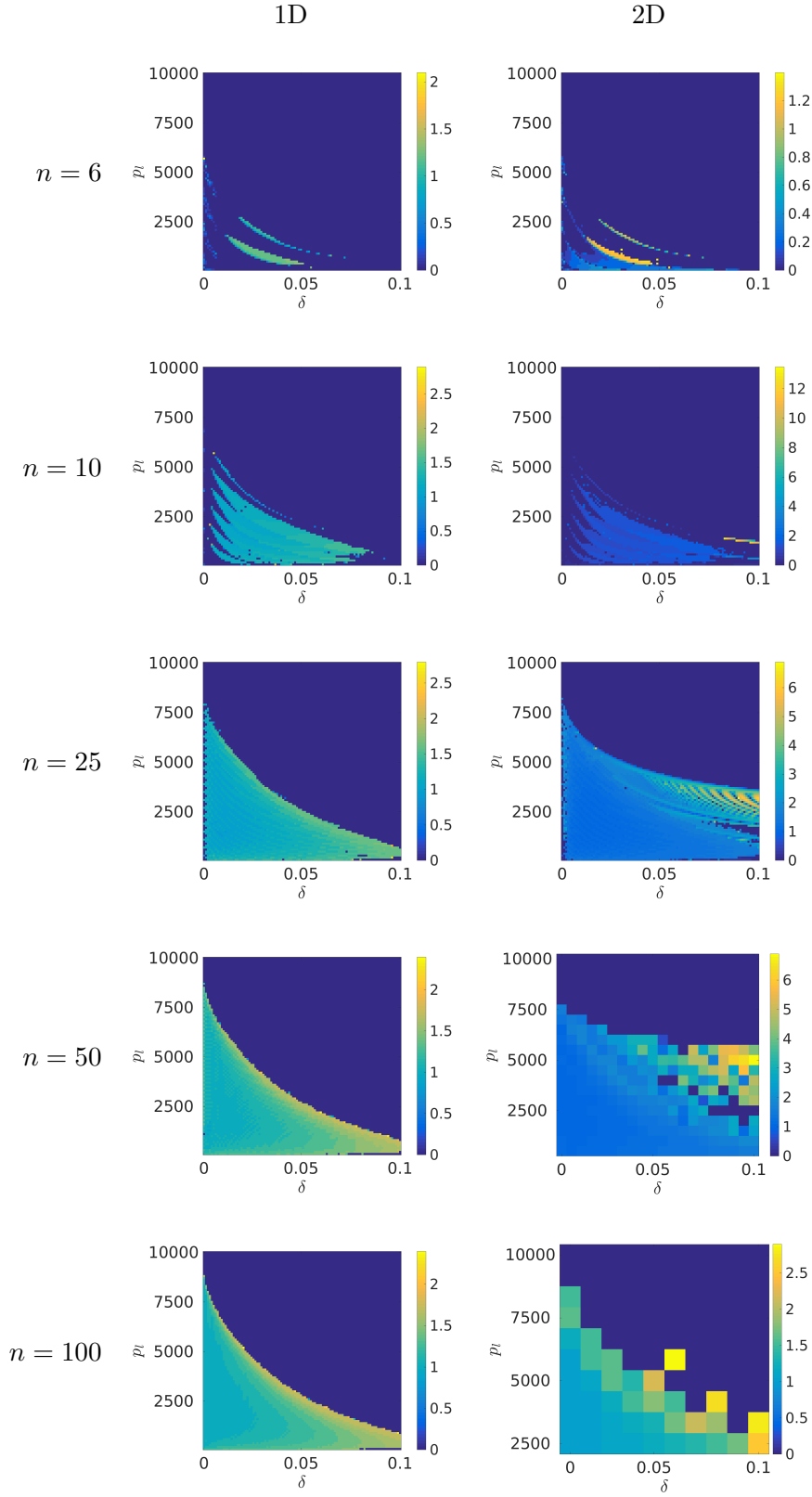


Figure 22: Frequency of the nodal oscillation after  $t = 40$  time units for different lattice sizes and dimensions over  $\delta$  and  $p_l$ .

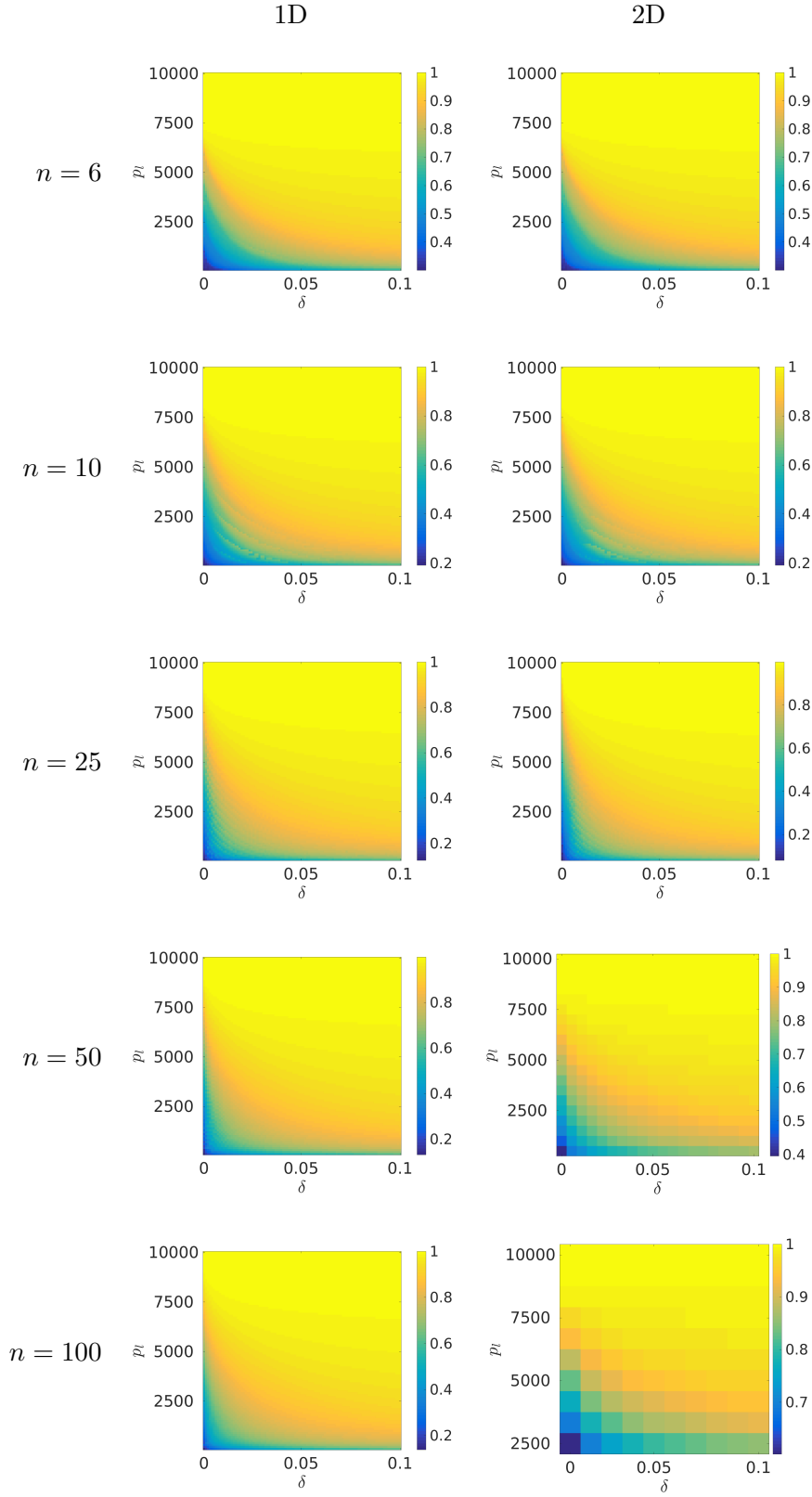


Figure 23: Mean cell density after  $t = 40$  time units for different lattice sizes and dimensions over  $\delta$  and  $p_l$ .

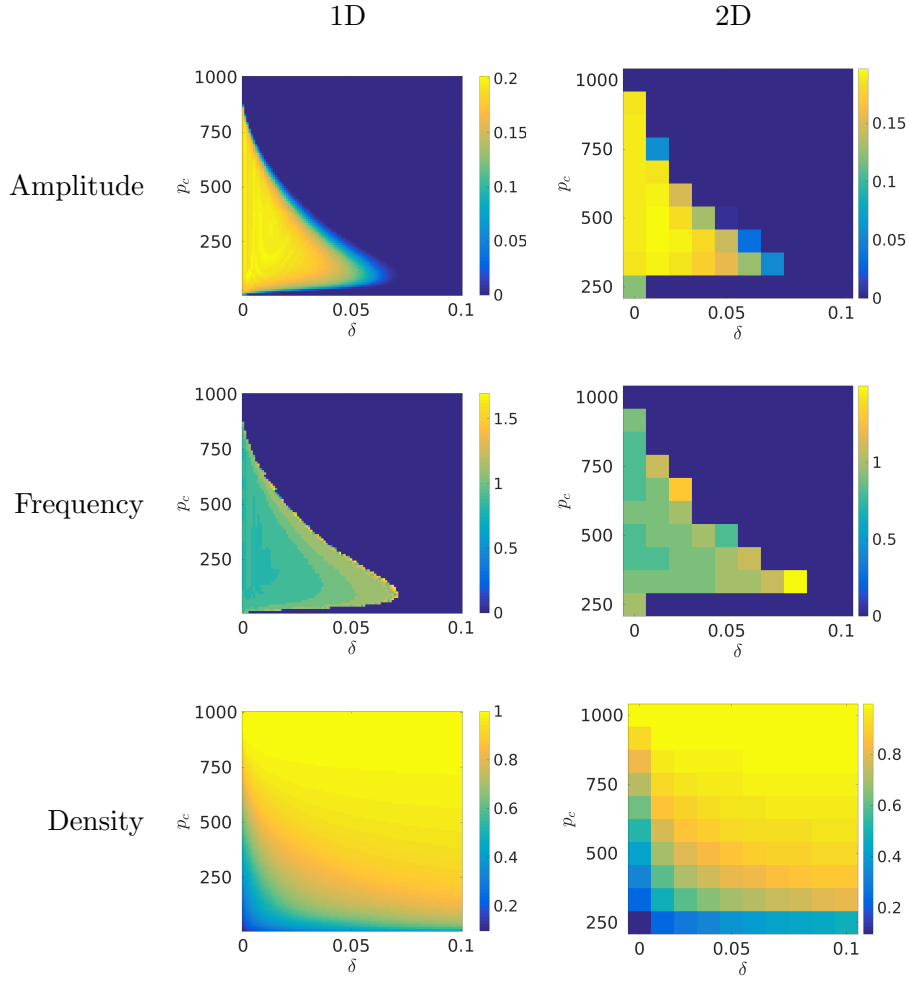


Figure 24: Bifurcation diagrams for the PDE and dimensions over  $\delta$  and  $p_c$ . Plotted in the first row is the amplitude, and the second the frequency of the maximal nodal oscillation after  $t = 40$  time units. The third row is the mean cell density.

have more complicated regions not present in the 1-D models where non-vertically-symmetric oscillations are present. The magnitude of the nodal oscillations away from the pulsing regime appears to decrease as a function of  $n$ , whereas the pulsing oscillations maintain a comparable amplitude for  $n \gtrsim 25$ . Similarly, the frequency of oscillations away from the small  $\delta$  or  $p_l$  regime increases with  $n$ . For the PDE, there is no appreciable difference between the 1-D and 2-D model behaviours. This gives further evidence that the symmetry-breaking oscillations of the smaller lattices disappear in the limit of  $n \rightarrow \infty$ . We note that the frequency of the oscillations increases with  $\delta$ , and is substantially larger for oscillations present in the 2-D lattices that are not present in their 1-D counterparts; compare the colorbar scales in Figure 22.

We can also consider the amplitudes of oscillations in the mean cell density over the entire lattice in Figure 25, in comparison to the maximal nodal oscillations plotted in Figure 21. We see no qualitative difference between the solutions of the 1-D and 2-D models, suggesting that for large  $n$ , the non-symmetric oscillations become less important in determining the magnitude of oscillations.

These results suggest that the non-symmetric oscillations in the smaller lattices are due to local symmetry-breaking bifurcations of Hopf type. For general differential-algebraic systems, Codimension-1 bifurcations can also be due to a singularity in the algebraic subsystem, or due to saddle-node bifurcations [27]. By the regularity of the graph Laplacian in (1), we conjecture that no singularity-induced bifurcations can occur. While we are unable to rule out saddle-node bifurcations, we do not observe them in any of our continuation studies. Nevertheless there are global bifurcations due to the changes in stability (or existence) of both kinds of oscillations. Specifically, the vertically-symmetric pulsing oscillations are not, as far as we can detect numerically, created via a Hopf or other local bifurcation from a steady state.

**6. Discussion.** In this paper we have presented and analyzed a variation on a pair of models we proposed in [12] that consider an active porous medium with interactions between cell growth and fluid flow. We have demonstrated several notable differences between the lattice models of various sizes, as well as the spatially continuous model.

In Section 2 we presented these models, and showed a particular simplification available in the case of vertically-symmetric cell density distributions. In Section 3, our numerical results showed that stable solutions to our models are either steady states or oscillations, either preserving or breaking vertical symmetry. Vertically symmetric solutions are robust to changing the boundary conditions and dimension of the models, as well as the size of the lattice above a minimum threshold. Non-vertically symmetric solutions appear in smaller lattices. In Section 4 we derived large diffusion asymptotics which recapitulates solution behaviours in these limits. This allowed us to confine parameter sweeps in Section 5 to reasonable ranges of the model parameters. We found that there is a region of parameter space for small diffusion parameters or small pressure thresholds where oscillations are observed. This region is relatively simple for large lattices, and for the continuum model, but for smaller lattices the parameter space is disconnected and contains both vertically symmetric and non-vertically symmetric oscillations. We also show that some non-vertically symmetric oscillations are due to local Hopf bifurcations from steady states, but that none of the vertically-symmetric oscillations are created from equilibria that we observed numerically.

Results in Sections 3 and 5 demonstrate an important role played by vertically symmetric steady states and oscillatory solutions to these models. Our numerical explorations show that in various limits, notably the large lattice limit of  $n \rightarrow \infty$ , these two solutions are the only stable asymptotic behaviours of the models for the parameters we explored. For smaller lattices we have shown the existence of Hopf and pitchfork bifurcations that break the symmetry of these solutions and give rise to non-symmetric steady states, and non-symmetric oscillating solutions. The phase space and the parameter space for medium-sized lattices ( $10 \lesssim n \lesssim 100$ ) appears to be difficult to analyze as it admits all of these various solutions, alongside what are complicated combinations of them as in Figure 7.

We interpret our results in terms of solution symmetry and nonlocal reaction-diffusion

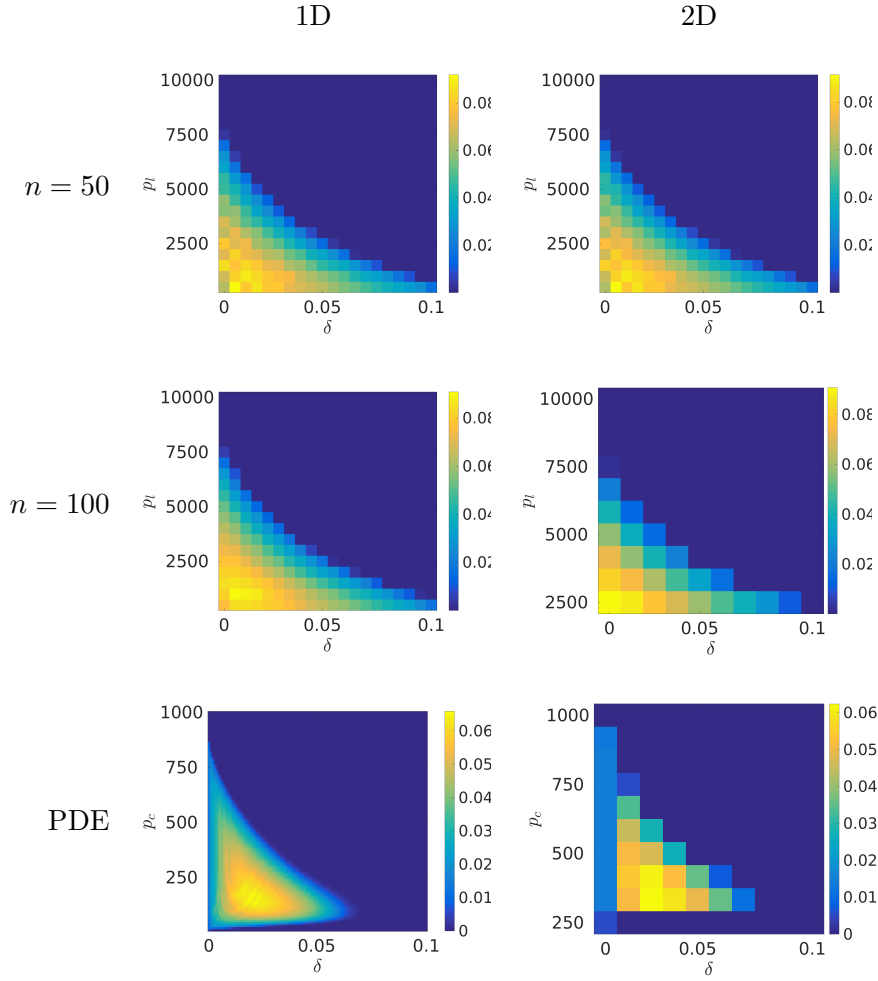


Figure 25: Amplitude of oscillations in the mean cell density after  $t = 40$  time units for different lattice sizes and dimensions over  $\delta$  and  $p_l$ .

mechanisms. Due to results from [15, 5], and others (see [23] for a more thorough review), it is known that scalar reaction-diffusion equations with Neumann data on a bounded domain have relatively simple asymptotic behaviour—namely, all bounded solutions converge to spatially uniform equilibria. Equation (19) is one simplification of our model that still admits spatially-structured and oscillatory solutions despite being a scalar reaction-diffusion equation. Simpler models of this kind have been considered in [10, 4, 13, 11], and the references therein, where oscillations and non-uniform equilibria are found and analyzed in models that are similar to Equation (20).

We conjecture that it is this inherently nonlocal structure, driven by the long-range quasi-static pressure forcing and short-range diffusion, that gives rise to all of the oscillatory behaviours we observe. For smaller lattices, the non-vertically symmetric steady states and

oscillations are related to symmetry breaking, namely a reflection symmetry about the horizontal axis characteristic of  $\mathbb{Z}_2$ -symmetric systems. We conclude that the oscillations are then an interplay of this symmetry breaking with the nonlocal mechanism described before. This provides an explanation for the oscillations found in [12], which we suspect is due to this interplay of nonlocality and symmetry. The decreasing effects of oscillations, and their absence in the continuum analogue, may be due to the shear-stress forcing on cell growth having localizing gradients in pressure. This is in contrast to the model presented here, where the pressure itself is forcing the cell growth problem.

In the context of bioactive porous media, these models demonstrate several interesting effects due to the finite pore network captured in our lattice model. In the limit of very large lattices, we suspect that spatially continuous models are good approximations to these kinds of pore networks, at least for the simple topology considered here. For smaller networks, we have demonstrated nontrivial effects due to the symmetries inherent in the network that cannot be captured in continuous analogues. We suspect that more realistic (and hence more complicated) pore networks may exhibit other behaviours due to the presence or lack of symmetries in the model. These are not readily captured in the spatially continuous model. Further explorations of network models of active media will be both quantitatively useful for porous media applications, and provide a number of interesting mathematical questions to pursue.

## REFERENCES

- [1] Y. BARBOTTEAU, J. L. IRIGARAY, AND J. F. MATHIOT, *Modelling by percolation theory of the behaviour of natural coral used as bone substitute*, Physics in Medicine and Biology, 48 (2003), pp. 3611–3623.
- [2] J. BEAR, *Dynamics of Fluids in Porous Media*, American Elsevier, New York, 1972.
- [3] T. BEARD, D. KASERMAN, AND R. OSTERKAMP, *The Global Organ Shortage: Economic Causes, Human Consequences, Policy Responses*, Stanford University Press, Stanford, Jan. 2013.
- [4] J. BILLINGHAM, *Dynamics of a strongly nonlocal reaction-diffusion population model*, Nonlinearity, 17 (2004), pp. 313–346.
- [5] R. G. CASTEN AND C. J. HOLLAND, *Instability results for reaction diffusion equations with Neumann boundary conditions*, Journal of Differential Equations, 27 (1978), pp. 266–273.
- [6] N. S. CHRISTODOULOU, *Discrete Hopf bifurcation for Runge-Kutta methods*, Applied Mathematics and Computation, 206 (2008), pp. 346–356.
- [7] F. COLETTI, S. MACCHIETTO, AND N. ELVASSORE, *Mathematical Modeling of Three-Dimensional Cell Cultures in Perfusion Bioreactors*, Industrial & Engineering Chemistry Research, 45 (2006), pp. 8158–8169.
- [8] S. C. COX, J. A. THORNBY, G. J. GIBBONS, M. A. WILLIAMS, AND K. K. MALICK, *3d printing of porous hydroxyapatite scaffolds intended for use in bone tissue engineering applications*, Materials Science and Engineering: C, 47 (2015), pp. 237–247.
- [9] C. L. GERMAN AND S. V. MADIHALLY, *Applications of Computational Modelling and Simulation of Porous Medium in Tissue Engineering*, Computation, 4 (2016), p. 7.
- [10] S. A. GOURLEY, M. A. J. CHAPLAIN, AND F. A. DAVIDSON, *Spatio-temporal pattern formation in a nonlocal reaction-diffusion equation*, Dynamical Systems, 16 (2001), pp. 173–192.
- [11] F. HAMEL AND L. RYZHIK, *On the nonlocal Fisher-KPP equation: steady states, spreading speed and global bounds*, Nonlinearity, 27 (2014), p. 2735.
- [12] A. L. KRAUSE, D. BELYAEV, R. A. VAN GORDER, AND S. L. WATERS, *Lattice and continuum modelling of a bioactive porous tissue scaffold*, Preprint, (2017).
- [13] E. A. LEVCHENKO, A. V. SHAPOVALOV, AND A. Y. TRIFONOV, *Asymptotics semiclassically concentrated on curves for the nonlocal Fisher-Kolmogorov-Petrovskii-Piskunov equation*, Journal of Physics



- A: Mathematical and Theoretical, 49 (2016), p. 305203.
- [14] Q. L. LOH AND C. CHOONG, *Three-Dimensional Scaffolds for Tissue Engineering Applications: Role of Porosity and Pore Size*, Tissue Engineering Part B: Reviews, 19 (2013), pp. 485–502.
  - [15] H. MATANO, *Convergence of solutions of one-dimensional semilinear parabolic equations*, Journal of Mathematics of Kyoto University, 18 (1978), pp. 221–227.
  - [16] P. MAAS AND B. M. MACKEY, *Morphological and Physiological Changes Induced by High Hydrostatic Pressure in Exponential- and Stationary-Phase Cells of Escherichia coli: Relationship with Cell Death*, Applied and Environmental Microbiology, 70 (2004), pp. 1545–1554.
  - [17] S. MCDUGALL, *Mathematical Modelling of Flow Through Vascular Networks: Implications for Tumour-induced Angiogenesis and Chemotherapy Strategies*, Bulletin of Mathematical Biology, 64 (2002), pp. 673–702.
  - [18] M. E. J. NEWMAN, *Networks: an introduction*, Oxford University Press, Oxford ; New York, 2010.
  - [19] K. H. L. NELER, J. R. HENSTOCK, A. J. EL HAJ, S. L. WATERS, J. P. WHITELEY, AND J. M. OSBORNE, *The influence of hydrostatic pressure on tissue engineered bone development*, Journal of Theoretical Biology, 394 (2016), pp. 149–159.
  - [20] R. D. O'DEA, H. M. BYRNE, AND S. L. WATERS, *Continuum Modelling of In Vitro Tissue Engineering: A Review*, in Computational Modeling in Tissue Engineering, L. Geris, ed., no. 10 in Studies in Mechanobiology, Tissue Engineering and Biomaterials, Springer Berlin Heidelberg, 2012, pp. 229–266.
  - [21] R. SEYDEL, *Practical Bifurcation and Stability Analysis*, Springer Science & Business Media, New York, Dec. 2009.
  - [22] M. SHAKEEL, P. C. MATTHEWS, R. S. GRAHAM, AND S. L. WATERS, *A continuum model of cell proliferation and nutrient transport in a perfusion bioreactor*, Mathematical Medicine and Biology: A Journal of the IMA, 30 (2013), pp. 21–44.
  - [23] H. L. SMITH, *Monotone Dynamical Systems: An Introduction to the Theory of Competitive and Cooperative Systems*, American Mathematical Soc., 2008.
  - [24] M. THULLNER AND P. BAVEYE, *Computational pore network modeling of the influence of biofilm permeability on bioclogging in porous media*, Biotechnology and bioengineering, 99 (2008), pp. 1337–1351.
  - [25] K. VAFAI, *Porous Media: Applications in Biological Systems and Biotechnology*, CRC Press, London, Aug. 2010.
  - [26] C. A. VAN BLITTERSWIJK AND P. THOMSEN, eds., *Tissue engineering*, Academic Press series in biomedical engineering, Elsevier, Acad. Press, Amsterdam, 2008.
  - [27] V. VENKATASUBRAMANIAN, H. SCHATTLER, AND J. ZABORSZKY, *Local bifurcations and feasibility regions in differential-algebraic systems*, IEEE Transactions on Automatic Control, 40 (1995), pp. 1992–2013.